International Communications in Heat and Mass Transfer 167 (2025) 109379

Contents lists available at ScienceDirect

International Communications in Heat and Mass Transfer

journal homepage: www.elsevier.com/locate/ichmt

Development and experimental investigation of a modular, honeycomb shell-and-coil PCM-based latent heat thermal energy storage unit assisted with heat pipes. Dynamic simulation of melting process by using object-oriented modeling

Michał Rogowski [a,*], Maciej Fabrykiewicz [b], Dietmar Kuhn [c], Elisabeth Schröder [c], Rafał Andrzejczyk [a,*]

[a] Gdansk University of Technology, Narutowicza 11/12, 80-233, Poland
[b] State University of Applied Sciences in Elbląg, Institute of Technology, Wojska Polskiego 1, 82300 Elbląg, Poland
[c] Karlsruhe Institute of Technology, Hermann-von-Helmholtz-Platz 1, 76344 Eggenstein-Leopoldshafen, Germany

ARTICLE INFO

Keywords:
Melting
Honeycomb-shell and coil
Thermal energy storage
PCM
Object-oriented modeling
Thermal resistance

ABSTRACT

This study investigates a modular latent heat thermal energy storage (TES) unit designed to enhance energy storage efficiency using coconut oil as the phase-change material (PCM). The research aims to address the challenge of efficient heat transfer in compact TES systems for applications like solar energy and waste heat recovery. The unit features a novel honeycomb shell-and-coil structure with aluminum helical coils and copper heat pipes, facilitating heat transfer to the PCM via circulated heat transfer fluid. Experiments were conducted under two regimes: 34.5 °C inlet temperature with 1.2 L/min flow rate and 33 °C with 1.7 L/min. Results demonstrate a volumetric energy density of 38 kWh/m^3 and a maximum charging rate of 0.5 kW. Performance was evaluated using the normalized heat transfer performance coefficient (NHTPC) and volumetric energy density (VED), showing competitive efficiency compared to other TES designs. A dynamic model, developed using object-oriented modeling in Modelica, accurately predicts temperature and heat flux, validated against experimental data with a maximum discrepancy of 6 %. This work introduces a scalable, modular TES design and a novel NHTPC vs. VED comparison methodology, offering significant potential for optimizing thermal energy storage systems in the future.

1. Introduction

Despite significant advancements TES technology is still in its early stages of development. Numerous research and development works are being carried out in various energy sectors to enhance the capacity and power output of TES systems. However, the integration of the TES units is a key element of proper utilization of many intermittent heat sources. Consequently, the use of PCMs to store thermal energy is a promising technology that has gained significant attention in recent years. PCM-based TES systems are capable of being used for applications with a very wide range of temperatures from refrigeration [1], heating, ventilation, and air conditioning [2] to thermal management of electric batteries [3], solar hot water systems [4], and waste heat recovery [5]. Despite their relatively high volumetric energy density compared to water, PCM-based TES systems still require a substantial storage material for industrial applications. This requirement is one of the reasons why researchers are exploring modular TES systems. These systems aim to maximize storage material packing within a confined volume while enhancing total heat capacity and power output of TES unit. Furthermore, studies have confirmed that modular storage maximizes enthalpic and energetic gain for storage [6].

Modular TES systems of various shapes have recently been studied. The research by K. Kant et al. [7] on honeycomb heat exchangers filled with PCMs demonstrated that cell shapes and arrangement significantly improve heat transfer. The authors used n-octadecane as the PCM and tested various configurations, including different fin thicknesses, sizes, and computational domains. Their findings show that inclination angles have minimal influence when cells are smaller than 0.01 m. Cell shape influences energy storage rates and liquid fraction dynamics, while

* Corresponding authors.
E-mail addresses: michal.rogowski@pg.edu.pl (M. Rogowski), rafal.andrzejczyk@pg.edu.pl (R. Andrzejczyk).

https://doi.org/10.1016/j.icheatmasstransfer.2025.109379

Available online 18 July 2025

Nomenclature

A	Surface area [m^2]
c_p	Specific heat capacity [J/kgK]
d, D	Diameter [m]
G	Thermal conductance [W/K]
h	Heat transfer coefficient [W/m^2K]
H_{ls}	Latent heat [kJ/kg]
M	Mass [kg]
$NHTPC$	Normalized heat transfer performance coefficient [kW/m^3K]
$\dot{Q}$	Heat flux [W]
R	Thermal resistance [K/W]
V	Volume [m^3]
VED	Volumetric energy density [kW/m^3K]
$\dot{V}$	Volume flow [m^3/s]
T	Temperature [K]
δ	Thickness [m]
ε_{avg}	Average heat exchanger effectiveness [−]
Φ_{PCM}	Packing factor [−]
λ	Thermal conductivity [W/mK]

Abbreviations

HP	Heat pipe
HTF	heat transfer fluid
LHTES	Latent heat thermal energy storage
PCM	Phase-change material
TES	Thermal energy storage

Subscripts

conv	convective
in	inlet
m	mean
out	outlet
PCM	Phase-change material
tot	total

reducing the front surface temperature, which are typically high. In the work of M. Abuşka et al. [8] several solar air collectors with different geometries were compared. Two collectors incorporated PCM, with only the first featuring a honeycomb core, while the third was a flat absorber plate. The study showed that the honeycomb core significantly enhances thermal conductivity, and thus reduces charging and discharging time. The authors reported the thermal efficiency improvement from 10 to 13.5 % for the honeycomb design. In a related study [9] the authors tested the same three types of solar heaters to investigate the thermal performance for variable air mass flow rates ranging from 0.008 to 0.048 kg/s. Results showed that PCM-equipped collectors experienced a performance decrease of approximately 7 % at low flow rates (up to 0.024 kg/s) and a slight reduction (~0.5 %) at higher rates (above 0.032 kg/s). The authors concluded that the honeycomb structure reduces charging and discharging times but marginally lowers daily thermal efficiency. The honeycomb structure of TES was considered also in the computational research by A. Andreozzi et al. [10]. Half of the cells were filled with PCMs and the rest were air zones in an alternating way on a checkerboard pattern. Two models were compared: a direct honeycomb structure and a porous medium model assuming local thermal equilibrium between solid and liquid phases They found comparable results for channels per unit length (CPL) above 4, attributed to increased heat transfer surface area. In a subsequent study [11], A. Andreozzi et al. numerically investigated the honeycomb PCM structures of PCM in solar energy systems, using paraffin wax and varying pores per unit length (PPL). Differences between the direct and porous models were significant at lower PPL values due to reduced heat transfer surface area. M. S. Mahdi and A. F. Hasan [12] numerically analyzed honeycomb heat exchangers with PCM and validated experimentally assessing various cell angles and HTF flow configurations. Their findings indicate that the honeycomb structure promotes uniform melting and solidification, though cell angles have a negligible effect on phase change speed. The multiple water block geometry, as well as the working fluid arrangement, affected significantly the influence of the processes inside the container. S. A. Sadri et al. [13] tested solar air heaters to optimize aluminum honeycomb core arrangements in TES, using numerical mass flow rates of 0.02 and 0.04 kg/s and experimental validation of PCM melting and solidification. The authors selected the most optimal configuration of the heat storage structure from several tested cases. The obtained results showed that the honeycomb core shortens the melting time by approximately 35 % and the most optimal arrangement can increase the charging speed of the energy storage by 50 % but reduces its density by about 2 %. R. Hirmiz et al. [14] in their investigation analyzed PCM-based TES integrated with heat pumps. They carried out numerical calculations and analytical predictions to optimize storage tank size. Their hybrid PCM-water design reduced tank volume by over three times while meeting household thermal energy demands during peak periods, and they proposed a simplified method for estimating storage volume. A. Gil et al. [15] investigated thermal conductivity enhancement in PCM-based TES, comparing two containers filled with hydroquinone, one with transversal, squared fins. Those fins increased thermal conductivity by ~26 % across various heat flow rates and inlet temperatures. S. Abbas et al. [16] used PCMs for thermal management system of lithium-ion batteries in electric vehicles. The authors carried out an experimental investigation of the cooperation of that system with PCM using paraffin as well as flat plate heat pipes. Attached heat pipes reduced module maximum temperature by 31 % at a 6 W heat flux, proving effective for thermal stabilization. In another experiment, G. Dogkas et al. [17] investigated the capabilities of thermal storage using filled with PCM cooperating with a heat source for domestic hot water production. The authors prepared a rectangular tank with a staggered finned heat exchanger inside. They tested two different phase change substances and analyzed the amount of hot water depending on the rate of melting and solidification of the substance and the density of stored energy. The melting temperatures of organic PCM (A53 and A58H) were 53 °C and 58 °C respectively. The tanks could be charged with heat in less than 2 h with heat flux above 5 kW. It was calculated that in one cycle the system could deliver about 106 l of domestic hot water with a temperature more than 40 °C which meets the requirements for residential use. R. M. Saeed et al. [18] tested plate-type heat exchangers in PCM-based TES, comparing 1-in. and 2-in. plate spacings. Compared to conventional TES systems the plate geometry with PCM demonstrates an efficiency of at least 83 % higher, where the more optimal plate-plate spacing was 1-in. which reduced and exited water temperature. This kind of upgrade in heat storage has a higher storage capacity maintaining its compact design. M. Fadl and P. C. Eames [19] experimentally analyzed RT44HC in a rectangular TES tank with a vertical multi-pass tube for domestic hot water. Increasing inlet temperature from 60 °C to 70 °C reduced charging time by 3.5 h, and to 80 °C by an additional 2 h; flow rates above 10 L/min had minimal impact. The solid layer of PCM around the tubes increased thermal resistance. In the experimental investigation, M. M. Joybari et al. [20] compared shell-and-tube heat exchangers with PCM, finding that multiple-tube designs significantly reduced charging and discharging times due to larger heat transfer surfaces and enhanced natural convection. Apart from that the authors concluded that increasing the working medium flow rate gives

Table 1
Thermophysical properties of coconut oil [26].

Property	Value	Unit
λ	0.329	W/mK
ρ	1130	Kg/m^3
h	178	kJ/kg
c_p	2.07	kJ/kg·K
T_m	25.5	°C
μ	0.02	Pa·s
ν	$1.77{\cdot}10^{-5}$	m^2/s
β	$7.61{\cdot}10^{-4}$	1/K
α	$1.4{\cdot}10^{-7}$	m^2/s
Pr	125.8	–

negligible improvement due to the turbulent flow regime inside the tubes. S. Tiari et al. [21] investigated a cylindrical TES with a heat pipe network and PCM (Rubitherm RT55), using high-velocity water as HTF. The results showed that the heat flow rate and the temperature of the HTF have a meaningful influence on the charging time of the device. Increasing the HTF from about 1,9 L/min to 7,6 L/min sped up the charging process by 30 % and increasing the temperature from 63 °C to 73 °C shortened it by another 55 %. However, in the case of discharging, only the temperature change matters. The study of S. Seddegh et al. [22] examined a cylindrical shell-and-tube TES, testing four tube radii to optimize shell-to-tube diameter ratios. Their results show that the diameter ratio of 5.4 minimized charging and storage time in the considered system. The mass flow rate has no significant meaning, but increasing its temperature from 70 °C to 80 °C reduced charging time by up to 68 %. M. Esapour et al. [23] numerically investigated multi-tube heat exchangers working with PCM. In four different configurations, they added the quantity of inner tubes inside the device. In the outer and inner tubes, the water was flowing through as HTF, and the rest of the tank was filled with PCM (RT 35). Increasing the inlet temperature reduced charging time, while the HTF rate increase has almost no effect on this process. Adding additional inner tubes from 1 up to 4 led to an enhancement in the heat transfer surface and thus increased the melting rate by 29 %. A. Pourakabar and A. A. Darzi [24] numerically analyzed melting and solidification in cylindrical TES with various tube arrangements. In the beginning, the melting process occurred mainly in the upper part of the storage, while in the lower part, a large amount of PCM remained solid. The vertical array of two tubes inside had a much higher melting rate than the single-tube set, whereas a two-tube horizontal array had a lot shorter solidification time than the four-tube rhombus configuration. In the next step, the authors inserted a copper foam inside the material to accelerate the phase change. It reduced the time melting time by 92 % and solidification time by 94 %, but it suppressed natural convection.

This literature review highlights a scarcity of experimental studies on modular TES systems, with most research focusing on single-unit cylindrical LHTES designs [25]. However, the modular LHTES seems to be more perspective especially due to the higher compactness and possibility to easily scalable heat power the accumulation system. Furthermore, in the context of geometry, the honeycomb structure has greater advantages. Geometry of TES module presented in the following article is an enhancement of a single cell shell-and-coil unit studied by authors [26]. This structure is lighter and has better mechanical properties than the other one.

Numerical studies prevail in this matter due to the cost reduction of the experimental facility, including the studied modular TES geometry. Significant advancements in numerical modeling have enhanced the understanding of phase change processes in TES systems. W. B. Ye and M. Arıcı conducted a comprehensive 3D validation and 2D feasibility study for pure solid-gallium phase change, demonstrating that 2D simulations can effectively reduce computational costs while maintaining accuracy [27]. In another study, they explored false diffusion, asymmetrical interfaces, and equilibrium states in gallium phase change, uncovering novel mechanisms for interface discrepancies [28]. Additionally, they redefined interface error metrics and performed 2D verification for gallium melting, achieving robust correlations with experimental data [29]. More recently, W. B. Ye and M. Arıcı developed a dimensionless correlation for the mushy zone constant in the enthalpy-porosity methodology, improving the accuracy of convection-diffusion modeling for calcium chloride hexahydrate melting in TES applications [30]. These studies collectively highlight the importance of rigorous numerical validation for optimizing modular TES designs.

This study introduces a novel modular, honeycomb shell-and-coil TES unit, enhanced with heat pipes and utilizing coconut oil as the PCM achieving a volumetric energy density of 38 kWh/m^3. Coconut's oil thermophysical properties are shown in Table 1. Unlike previous research focusing on single-unit cylindrical TES systems, such as shell-and-tube designs [22], this work advances the field by developing a scalable, compact modular system that integrates aluminum coils and copper heat pipes to enhance heat transfer efficiency. In contrast to Kant et al. [7], who explored honeycomb heat exchangers filled with PCM (n-octadecane) and noted the influence of cell geometry on heat transfer, our study incorporates heat pipes to improve vertical temperature uniformity, addressing limitations in heat transfer rates for smaller cells. This ensures more consistent melting across the module, enhancing system performance for low-temperature applications. The proposed design extends the NHTPC vs. VED comparison methodology introduced by Delgado-Diaz et al. [31], providing a robust framework for evaluating TES performance across diverse operating conditions. Compared to Abuska et al. [9], which investigated PCM-filled solar air collectors with honeycomb cores and reported a 13.5 % improvement in thermal efficiency, our modular TES design achieves greater scalability and heat transfer uniformity through the integration of heat pipes, making it suitable for applications like solar energy storage and waste heat recovery. The comprehensive experimental database, coupled with a validated object-oriented Modelica model exhibiting a maximum discrepancy of 6 %, offers a reliable tool for designing and optimizing future TES systems. This model is based on own simple modeling procedure based on total thermal resistance concepts adopted from the author's previous works [32]. This work addresses a critical gap in the literature, which lacks experimental studies on modular TES designs [25], thereby contributing significantly to the development of efficient, scalable thermal energy storage technologies for sustainable energy applications.

2. Experimental setup

An eight-cell hexagonal, modular TES system (1) was connected to the primary HTF loop system with propylene glycol as a working medium. The working medium is heated or cooled to the set temperature (depending on the melting or solidification process) in the temperature stabilizer (2). Temperature stabilizer (2) was especially manufactured, according to the main author's requirements equipped with a cooling system and an additional 200 l accumulation tank. It is also equipped with additional electric heaters for better stabilization of the outlet fluid temperature. The system is controlled by PLC and the accuracy of temperature is close to ±0.5 K. After leaving the stabilizer (2) HTF flows through the coils located in the heater tank (6). The heater tank consists of a tank filled with 60 l of water and five immersion heaters, each with 1400 W of heating power. After leaving the heater tank (6) HTF flows through the helical coils of the modular TES (1), which have been connected in series so that the glycol from one helical coil goes to the next. The movement of HTF was forced by the pump (3). The amount of medium flowing through the module (1) is regulated by a #1 bypass valve (5). The test stand allows the heater (6) to be omitted through a #2 bypass valve (7). After supplying or receiving heat to the PCM located in the TES module, the working medium returns to the temperature stabilizer (2). The secondary loop consists of the HP flow channel (8) connected to the circulation loop of the Julabo Corio CD ultra

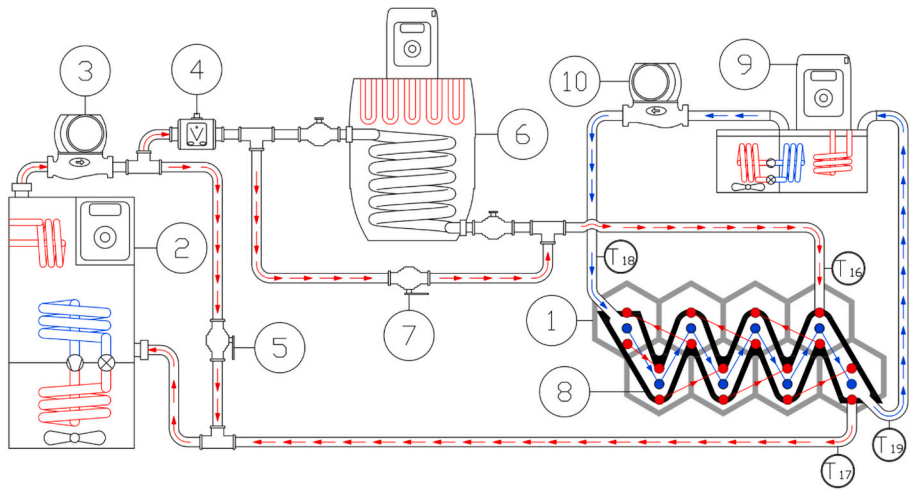

Fig. 1. Schematic representation of test stand; 1 – hexagonal, modular TES system, 2 – temperature stabilizer, 3 – primary loop's pump, 4 – flowmeter, 5 – #1 by-pass valve, 6 – heater, 7 - #2 by-pass valve, 8 – HP flow channel, 9 – secondary loop's ultra thermostat, 10 – built-in ultra thermostat's circulation pump.

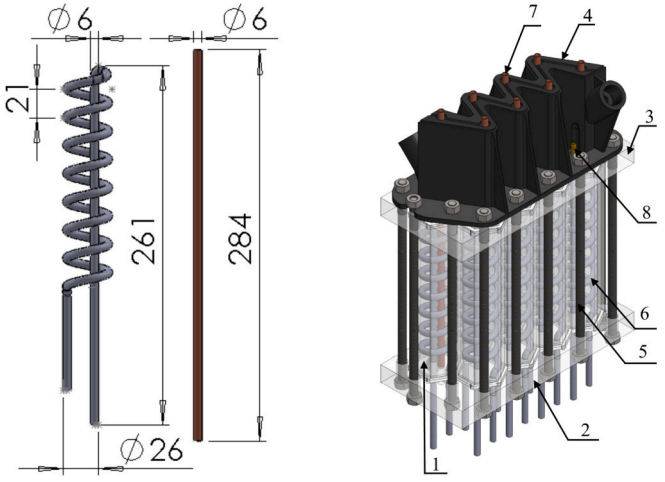

Fig. 2. Overall dimensions of helical, aluminum coil, and copper HP – left. Fully assembled hexagonal, modular TES and its components; 1 – shell, 2 – lower flange, 3 – upper flange, 4 – HPs flow channel, 5 – M8 threaded rod, 6 – aluminum coil, 7 – copper HP, 8 – M8 hex nut – right.

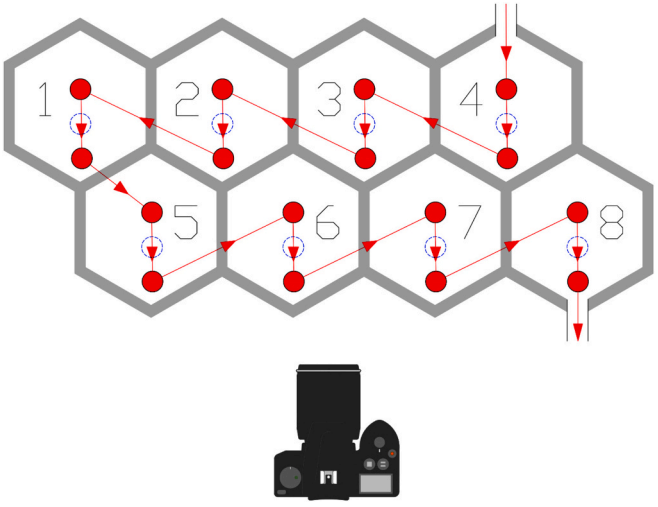

Fig. 3. Schematic representation of flow pattern of HTF, cell numeration, and photographic camera location of hexagonal, modular TES system, HPs' location was shown using blue, dotted line. (For interpretation of the references to colour in this figure legend, the reader is referred to the web version of this article.)

thermostat (9) which is equipped with a built-in circulation pump (10). The secondary loop's ultra thermostat (9) is additionally equipped with a cooling system that allows it to achieve the set temperature of the working medium. The mass flow rate of the primary loop's HTF is measured by a MIM Kobold electromagnetic flowmeter (4). Temperatures at both the inlet and outlet of the modular TES system (1) and the HP flow channel (8) are measured using Pt100 resistance temperature sensors with an accuracy of ±0.2 °C. In order to visualize the dynamics of the melting and solidification process occurring in the eight-cell modular TES system, an IR C3 FLIR thermal imaging camera and an HD camera UI-1220ME-C-HQ camera with 752 × 480 pixel resolution equipped with Pentax H1214-M lens were used. All temperature sensors, pressure transducers, and flow meters were connected to the National Instruments eDAQ-9189 data acquisition system with LabVIEW software. The diagram of the test stand is shown in Fig. 1.

Fig. 2. illustrates a 3D view of the hexagonal, modular TES system. This system consists of an eight-cell thermal module, also called shell (1), lower (2), and upper (3) flanges, and a flow channel (4) placed above the upper flange (3). The entire set was assembled using twelve M8 threaded rods (5) and M8 hex nuts (8). The shell (1) consisted of eight honeycomb-shaped cells arranged in two columns of four cells each, which were separated by a wall. Each cell of the shell contained a helical coil made out of 6 mm aluminum tube with a 1 mm thickness (6) placed perpendicular to the flanges. Coils were connected in series.

The HTF flow pattern through the helical coils located in the shell is shown in Fig. 1, but a close-up of this pattern is also shown separately in Fig. 3 for clarity. Cell numbering is also shown in Fig. 3.

The purpose of the HPs flow channel (4) was to allow for the secondary loop's HTF to supply or receive heat from in-house manufactured copper HPs (7) placed along the shell, one for each cell. Those heat pipes consisted of a 6 mm copper tube with a 1 mm thickness. Capillary structure was made out of a copper mesh with a mesh width of 130 μm, a mesh height of 120 μm, and a wire thickness of 70 μm. Working fluid for those heat pipes was acetone, which was determined to occupy 36.6 % of the heat pipe inner volume. This means that each heat pipe consisted of 1.1 g of acetone. The manufacturing process and performance evaluation of those heat pipes and their performance evaluation are described in more detail in the authors' previous work [33]. The purpose of HPs was to equalize the temperature in the PCM in the vertical

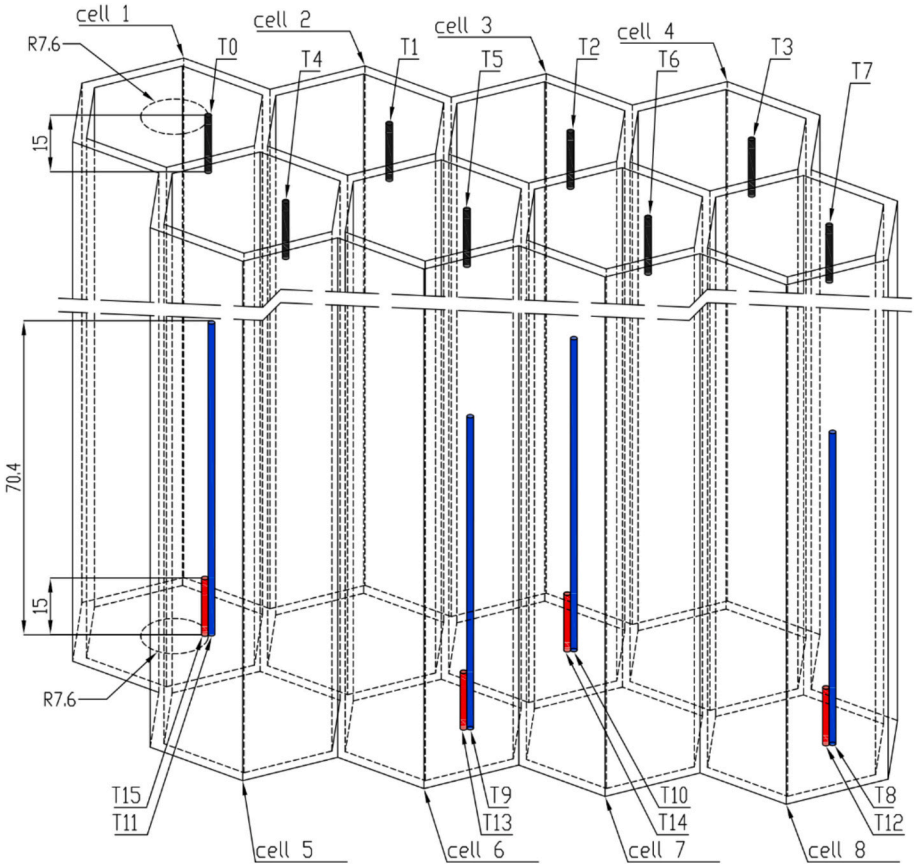

Fig. 4. Location of temperature sensors within the TES system's shell.

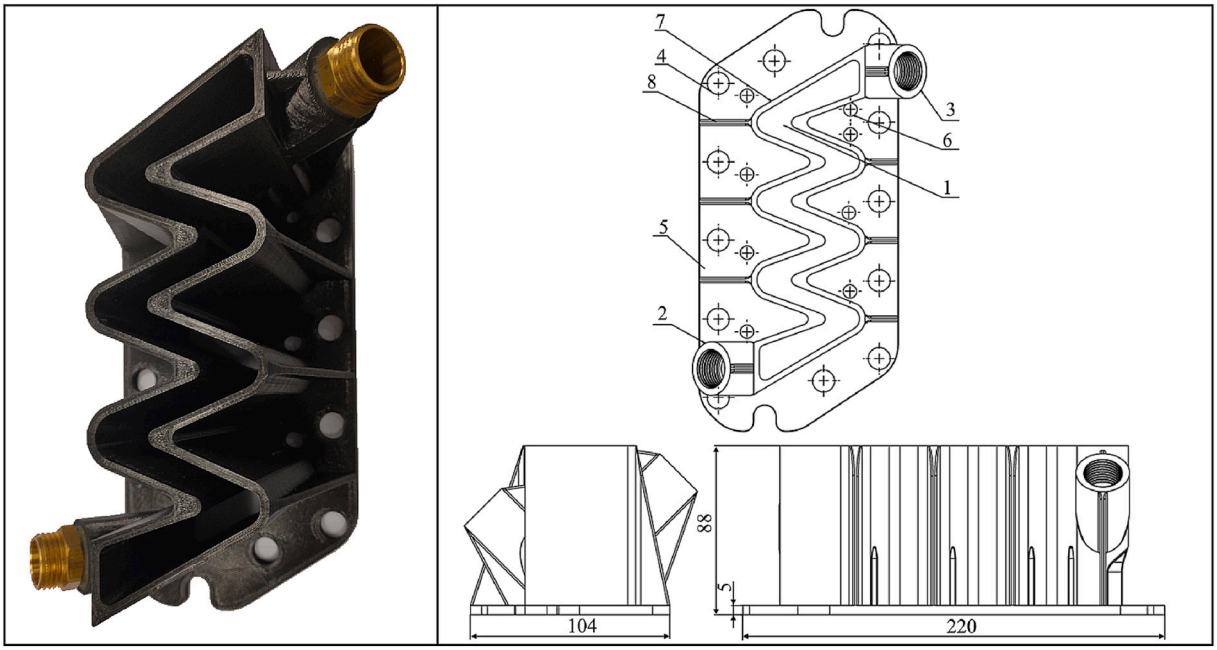

Fig. 5. Description of flow channel; top view without the top lid– left, orthogonal projections with dimensions – right; 1 – flow channel, 2 – inlet, 3 – outlet, 4 – mounting hole, 5 – base, 6 – hole for PCM filling, 7 – walls of the flow channel, 8 – fins.

direction. In order to maintain an appropriate fit ensuring tightness, special grooves reflecting the shape of the shell were milled in both the lower (2) and upper flanges (3). Grooves were additionally sealed with a special silicone gasket. The shell (1) was made as a monolithic element using FDM 3D printing technology. It was 3D printed using a translucent PET-G filament. This solution enabled the observation of the movement of the transition layer (liquid/solid). Drain holes were located in the lower flange (2) to enable the draining of the module of PCM. Lower (2)

Table 2
Uncertainties of measuring devices and calculated parameters.

Parameter	Operating range	Unit	Uncertainty
T_{PCM}	283.15–333.15	K	± 0.3 K
T_{HTF}	283.15–333.15	K	± 0.05 K
$\dot{V}$	0–10	L/min	± 0.5 %
p	0–16	bar	± 0.5 %
$\dot{Q}$	0–300	W	± 5 W

and upper flanges (3) were machined on a 20 mm thick acrylic glass board using a CNC milling machine. Pt100 resistance thermometers were soldered in pairs into threaded stubs and then screwed into specially drilled holes made in the lower flange (2), one hole for the two outermost and two inner cells. In the case of the upper flange (3), threaded holes were made for mounting connectors for filling individual cells (one for each cell), and special channels were drilled to enable the installation of thermometers. The location of thermometers within the shell and their respective numeration are shown in Fig. 4.

The HPs flow channel was 3D printed using PLA filament. Copper HPs are embedded in the HPs flow channel and reach the bottom of the shell. (see Fig. 2). Each copper HP is equipped with a pressure transmitter to enable pressure measurements inside HPs for their performance evaluation during the experiment. Two types of pressure transmitters were used, namely: NPXG16 Peltron relative pressure transmitters (cells 1, 2, 4, 5, 7, 8) and NPXA16 Peltron absolute pressure transmitters (cells 3, 6). Fig. 5 shows the view and a schematic of the flow channel. In order to supply or receive heat to/from the heat pipes, a flow channel (1) was designed, which was made using 3D printing technology using PLA as a 3D printing material. Both the inlet (2) and outlet (3) of the channel are equipped with G1/2″ nipples. In the base of the flow channel (5), there are 12 mounting holes (4) made to connect the channel with the TES unit and 8 holes for PCM filling (6) into the TES cells. To increase the stiffness of the structure, fins (8) were used to connect the base of the channel (5) with the walls (7).

The uncertainties of the measured parameters are given in Table 2.

3. Results of experimental investigation

The experiment was conducted under two distinct regimes: the first with a constant inlet temperature of 34.5 °C and a volumetric flow rate of 1.2 L/min, and the second with a constant inlet temperature of 33 °C and a volumetric flow rate of 1.7 L/min. Those two volumetric flow rates were chosen deliberately to fall within the range used in automotive air-conditioning systems [34]. These two experimental regimes are referred to as “1.2 lpm” and “1.7 lpm” further in the article. For both heat pipe’s pressure and temperature curves of “1.2 lpm” regime a solid line is used, while for “1.7 lpm” regime a dashed line is used on the graphs. Values of temperatures for each temperature sensor at a specific time were put into tabular data in Attachments: 1, 2, 3 and 4.

3.1. Variation in pressure during charging and discharging

Sub-pressures and absolute pressures of heat pipes located in cells: #1 to #8 for both experimental regimes are shown in Fig. 6 on left and right side respectively. The heat pipes, consisting of copper tubes, copper mesh, and acetone as the working fluid, were manufactured in-house by the research team Slight variations in operating pressures are expected due to temperature changes in the coconut oil PCM surrounding the heat pipes, which affect the temperature of the heat pipes’ working fluid. The primary role of heat pipes application inside the thermal

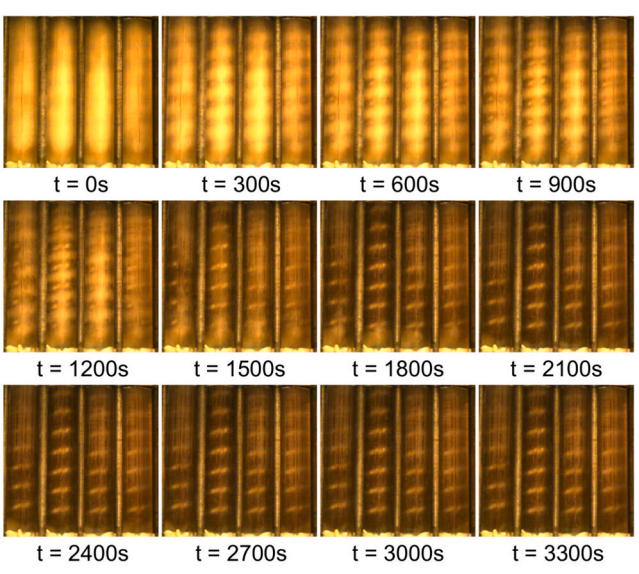

Fig. 7. Photos of the thermal module during the melting process along with respect to time.

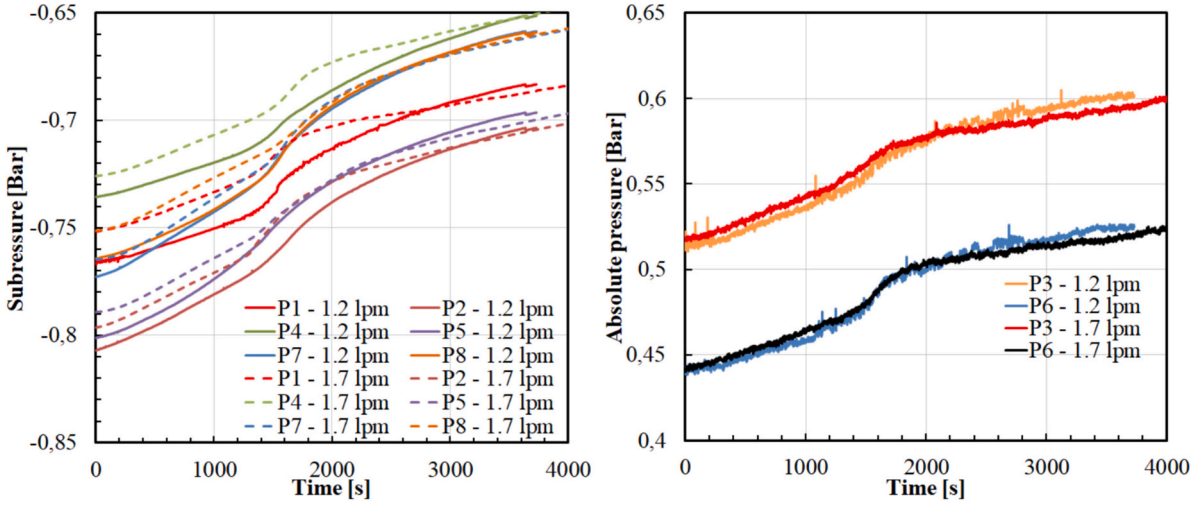

Fig. 6. Subpressure distribution (left) and absolute pressure distribution (right) vs. time respectively in cells: #1 to #8.

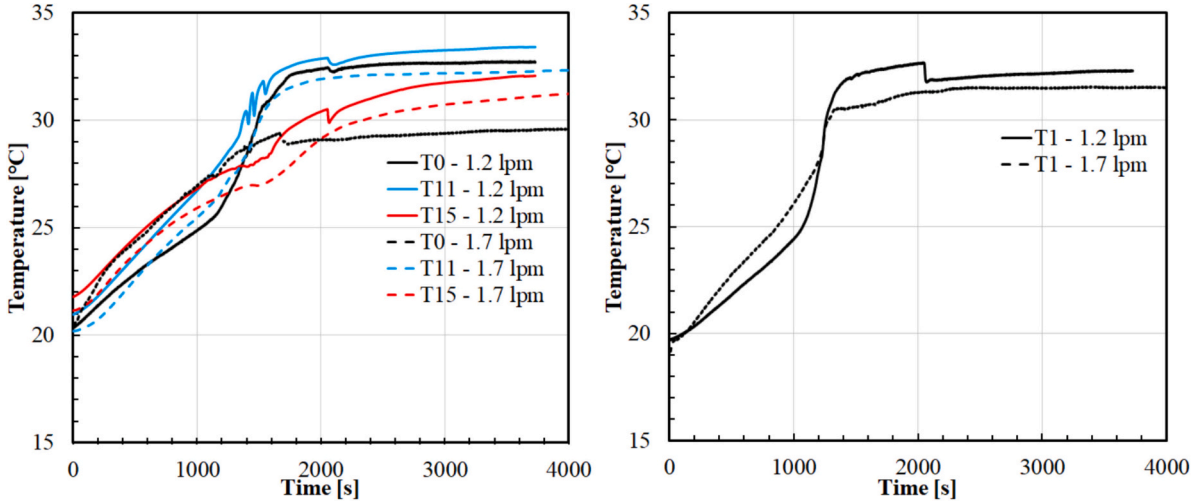

Fig. 8. Temperature vs. time distribution in cell #1 (left) and temperature vs. time distribution in cell #2 (right).

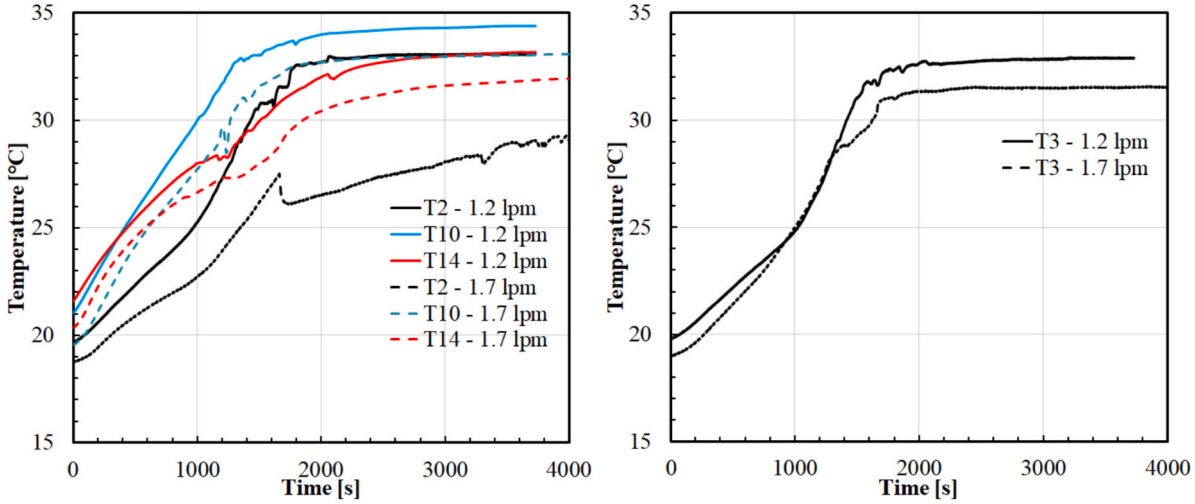

Fig. 9. Temperature vs time distribution in cell #3 (left) and temperature vs. time distribution in cell #4 (right).

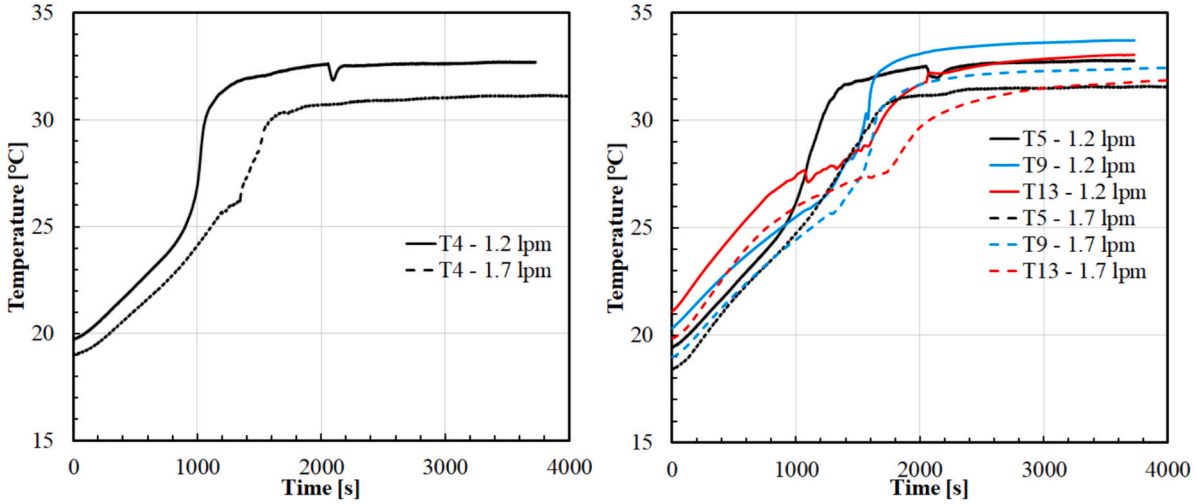

Fig. 10. Temperature vs. time distribution in cell #5 (left) and temperature vs. time distribution in cell #6 (right).

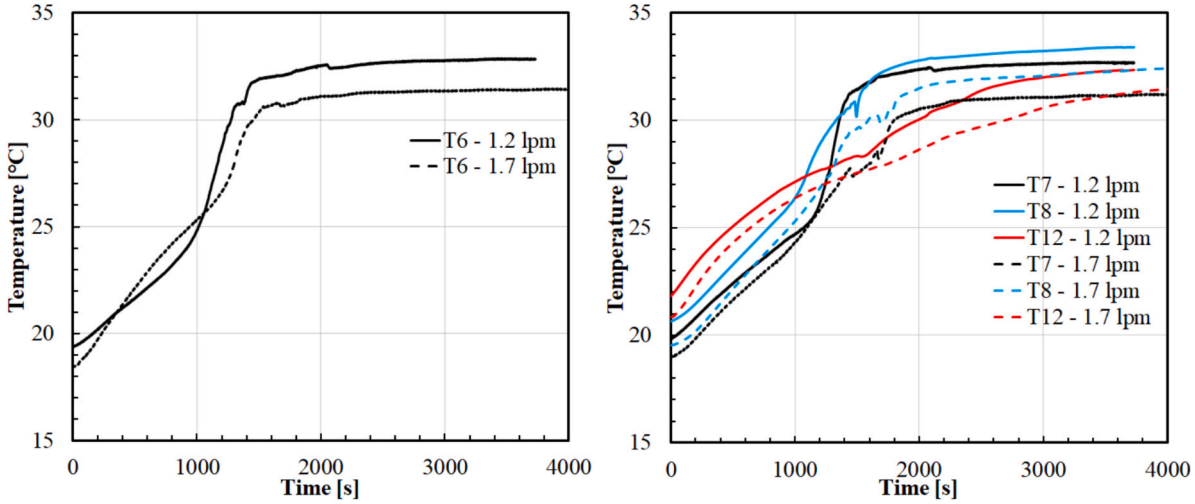

Fig. 11. Temperature vs. time distribution in cell #7 (left) and temperature vs. time distribution in cell #8 (right).

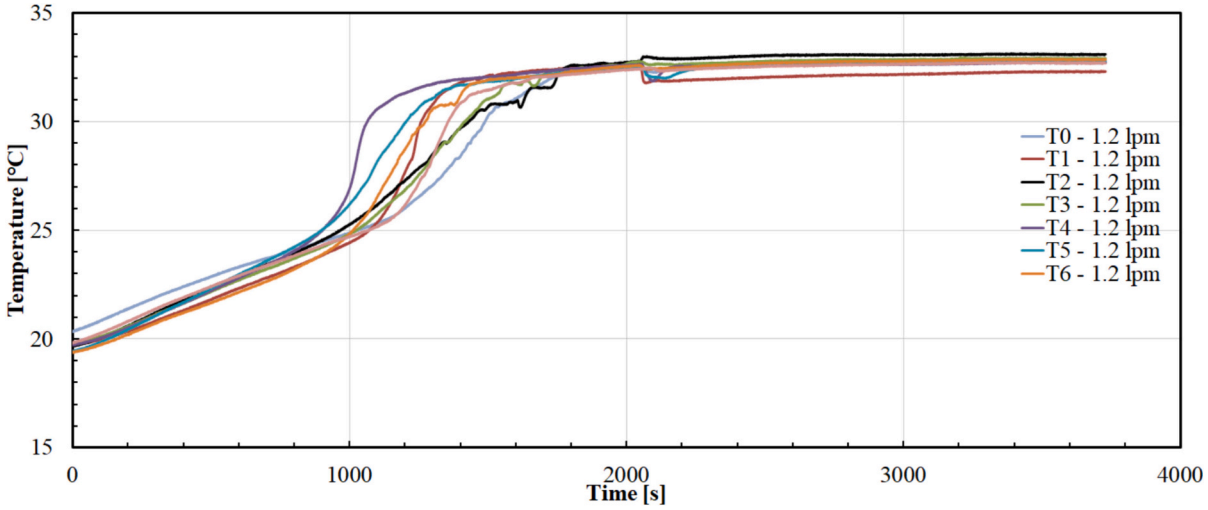

Fig. 12. Temperature vs. time distribution in all cells for "1.2 lpm" experimental regime.

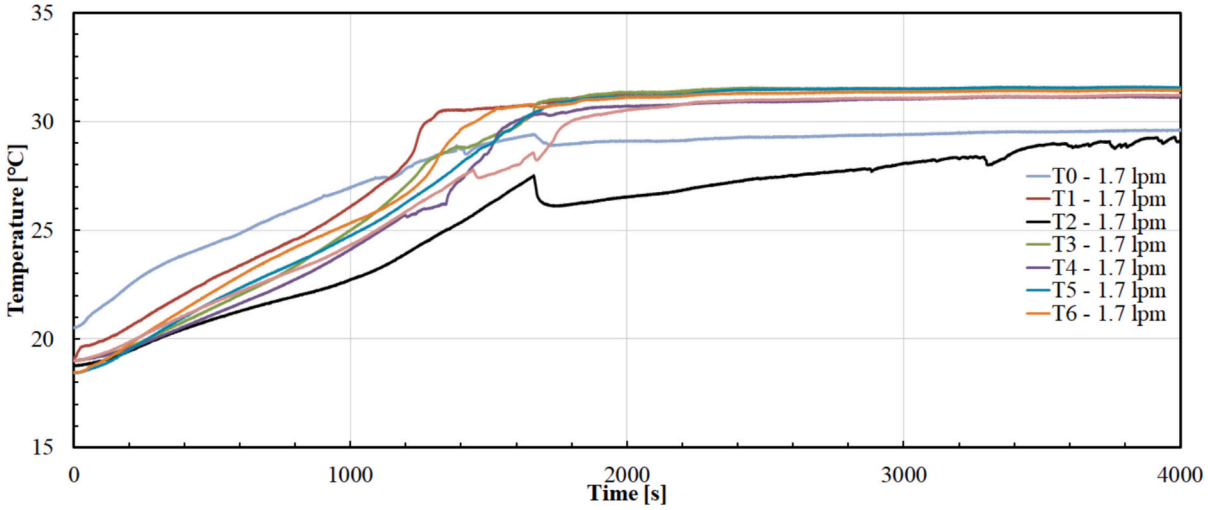

Fig. 13. Temperature vs. time distribution in all cells for "1.7 lpm" experimental regime.

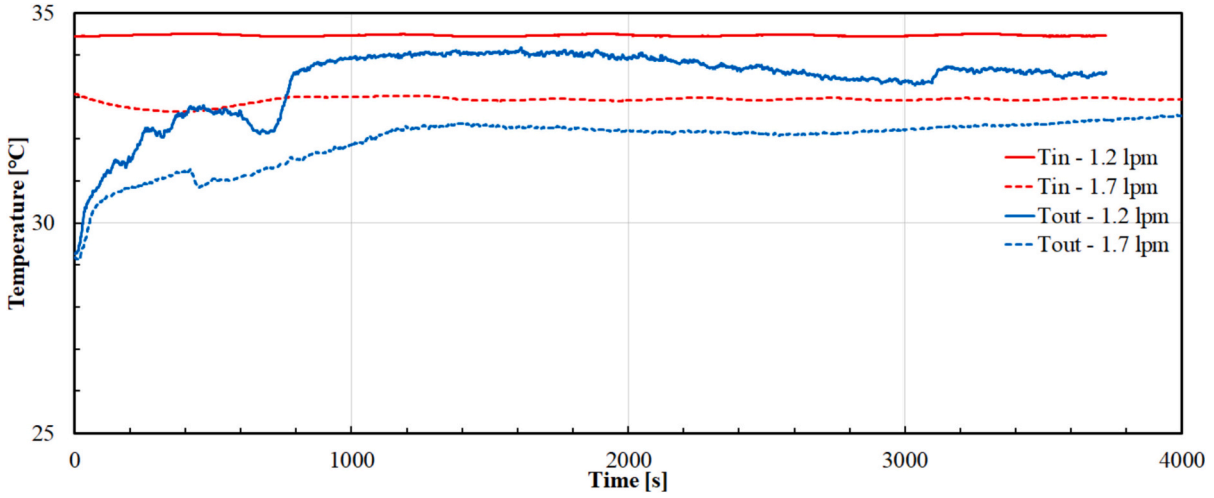

Fig. 14. Temperature measurements in the inlet (red) and the outlet (blue) of the thermal module for both experimental regimes. (For interpretation of the references to colour in this figure legend, the reader is referred to the web version of this article.)

module is to further enhance the heat transfer process within the coconut oil and uniform the temperature along the individual cell's height. Pressure profiles for both experimental regimes exhibit similar characteristic during melting.

3.2. Visual observations

Referring to the area covered by the camera, shown in Fig. 3, cells: 5, 6, 7, and 8 were observed through the camera during the experiment. Despite efforts to ensure the highest possible quality light illumination, the walls of the thermal module can be seen as translucent in the photos. This is due to the nature of 3D printing technology (deposition of molten filament layer by layer) and the semi-transparency of the 3D printing filament itself. As can be seen in Fig. 7., after about 300 s, PCM near the coils can be observed to be melted. Over time, the PCM melting process inside the thermal module occurs in a fairly uniform manner in all observed cells. After roughly 2100 s most of the PCM volume is melted along the height of the module, but there still exists a solid fraction of coconut oil at the bottom of the tank. This solid chunk takes the longest to melt. The melting process of the rest of the solid PCM ends after around 3000 s. For a more thorough analysis of over 8000 photos (each photo taken every 0.5 s) during the experiment, a simple program in Python 3.10.0 was written to join the photos into a timelapse video. This video is available at https://youtu.be/34rUo9CHNgA. The frame rate for this video was set to 450FPS. A comprehensive analysis of the video allowed us to grasp the movement of PCM, normally intangible to the human eye. During melting, small solid coconut oil fragments detach from larger chunks trapped between coil turns, sinking to the cell bottom due to density differences. These small fragments that drown to the bottom of the cell accumulate into a big chunk and take longer to melt than the rest of the PCM volume. This video also shows the upward movement of the liquid front. This can also be seen in the temperature vs. time graphs shown in the figures. Video as well as photos show that there is a slight non-uniformity of performance of individual cells. It takes the longest time for cell #5 to melt the remaining solid chunk at the bottom of the cell, in comparison with other cells.

3.3. Thermal analysis

Temperature distributions in individual cells are shown in Fig. 8, Fig. 9, Fig. 10 and Fig. 11. Colors of respective curves correspond to colors of temperature sensors schematically shown in Fig. 4.

As can be seen in Fig. 12**.** the temperature distribution of PCM in the upper parts is roughly uniform across all the thermal module cells for "1.2 lpm" regime.

As can be seen in Fig. 13**.** temperature varies significantly during the

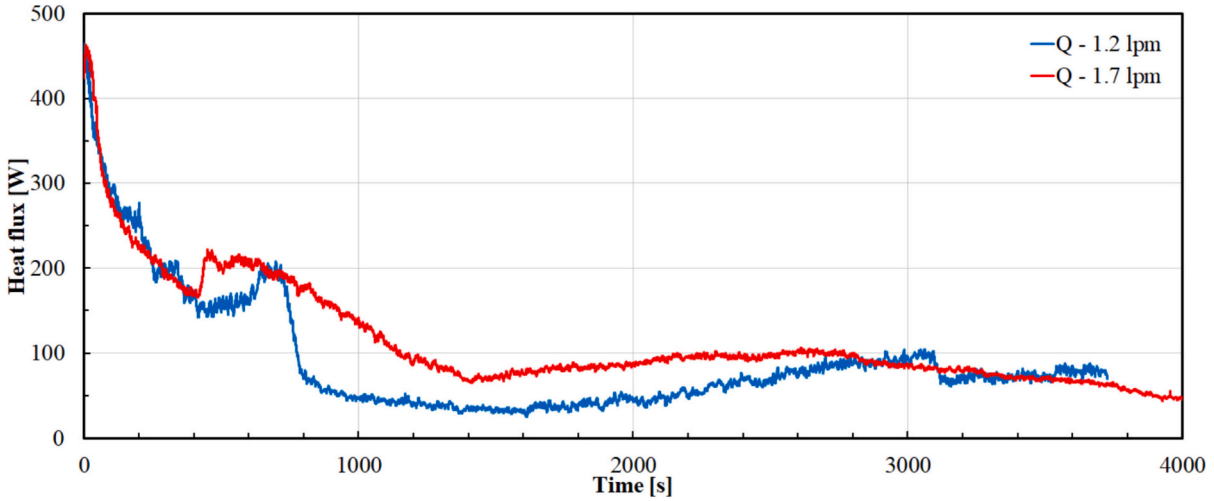

Fig. 15. Variation of average heat flux during the charging process.

melting process.

It is believed that the temperature difference between the inlet and outlet of the thermal module during the experiment can be attributed to heat losses between the outlet of cell #8 and the location of outlet temperature sensor T_17. It appears to be confirmed when looking at the temperature distribution of cell #8 shown in Fig. 11. The difference between the single-cell temperature stabilization time (approximately 1200 s) and the total melting time (approximately 3000 s) reflects a two-phase thermal response in the modular TES system. The initial 1200 s corresponds to rapid sensible heat absorption and the onset of phase change in the coconut oil PCM, driven by high temperature gradients near the helical aluminum coils and enhanced by copper heat pipes. However, the extended melting time of 3000 s results from slower melting of residual solid PCM fractions, particularly at the bottom of the honeycomb cells, where natural convection is less effective due to density-driven settling of solid PCM chunks, as observed visually (Section 3.2). This prolonged melting phase indicates that the system is better suited for applications requiring sustained heat storage and release, such as solar energy systems or waste heat recovery, rather than those demanding rapid heat transfer, such as instantaneous hot water supply. To improve suitability for quick-response applications, future designs could incorporate heat transfer enhancements, such as optimized coil geometry or introduction of finned coil [35], to accelerate melting in lower cell regions, potentially reducing the total melting time and enhancing overall thermal response [22].

The slight temperature difference between the inlet (T16) and outlet (T17) of the TES module, as shown in Fig. 14, is primarily due to heat losses between the outlet of cell #8 and the outlet temperature sensor (T17). These losses likely result from inadequate insulation of the TES unit's walls, particularly under the 1.7 L/min flow regime where higher flow rates increase heat dissipation. This inefficiency reduces the effective heat transfer to the coconut oil PCM, lowering the system's overall thermal performance and potentially affecting its energy storage capacity. This, however, was necessary to allow for the observation of melting through the semi-transparent walls of 3D printed hexagonal shell. To mitigate this problem a thicker wall of the shell could be implemented in the next version of the prototype.

3.4. Charging power behavior

Fig. 15 illustrates variations in heat flux $\dot{Q}$ during the charging process for both regimes. Initially, large temperature differences result in high heat flux, which decreases rapidly and stabilizes after approximately 300 s. This stabilization marks starting point of the melting process and an effect of heat transfer intensification by increasing the role of natural convection. After a stabilization period, the heat flux slowly drops till about 1500 s. It is because of the visibly decreased amount of solid phase in TES cells. As mentioned before after 2100 s most of the solid fraction is deposited at the bottom of honeycomb cells. However, there was also a slight disproportion with melting front geometries between different cells. Due to that fact till the moment of fully melted PCM still, some potential for heat accumulation can be observed (heat flux equal to about 50 W). In such a stage most of the PCM material has reached an equilibrium temperature close to the temperature of the heat transfer surface (see temperature graphs in Chapter 3.2). Residual solid phase at the bottom of the cells is slowly melted by convective currents till about 2700–3000 s. After that period heat flux steadily decreases.

3.5. Summary

Visual observations and temperature measurements (Fig. 8, Fig. 9, Fig. 10 and Fig. 11 in Section 3.3) indicate slight non-uniformity in melting performance across the eight cells of the modular TES module, with cell #5 exhibiting a notably slower melting rate, particularly for solid PCM fractions at the bottom (see Fig. 7). This disproportion likely arises from uneven HTF flow distribution through the series-connected helical coils or minor geometric variations in cell #5 introduced during the 3D printing process. Such inconsistencies can reduce overall system efficiency by delaying complete phase change and may compromise reliability, as uniform melting is essential for consistent energy storage and release in TES applications. To address this, future designs could incorporate parallel HTF flow paths to ensure even heat distribution across cells or implement stricter quality control during cell fabrication to minimize geometric deviations. These improvements, as demonstrated in similar studies on multi-tube TES systems [20], could enhance melting uniformity and optimize the system's performance for scalable applications like solar energy storage.

Table 3
Parameters for *NHTPC* and Φ_{PCM} calculations.

Exp. regime	$\dot{m}_{HTF}$ [kg/s]	$c_{p,HTF}$ [kJ/kgK]	V_{TOT} [m^3]	$\overline{T_{HTF,in}}$ [°C]	$\overline{T_{HTF,out}}$ [°C]	T_{PC} [°C]	V_{PCM} [m^3]
"1.2 lpm"	0,0202	4,19	0,0019	34.5	33.4	26.0	0,0016
"1.7 lpm"	0,0275	4,19	0,0019	33.0	32.0	26.0	0,0016

4. Key performance indicators

This study evaluates the performance of a modular, honeycomb shell-and-coil thermal energy storage (TES) unit using the normalized heat transfer performance coefficient (*NHTPC*, expressed in $\frac{kW}{m^3K}$) and volumetric energy density (*VED*, expressed in $\frac{kWh}{m^3}$), comparing it with 32 configurations studied W. Delgado-Diaz et al. [31]. The *NHTPC*, quantifies heat transfer efficiency relative to the total volume of the TES unit, enabling comparisons across diverse geometries and operating conditions. It is defined as:

$$\mathrm{NHTPC} = \frac{-\ln(1-\varepsilon_{avg}) * \dot{m}_{HTF} * c_{p,HTF}}{V_{TOT}} \ [-] \tag{1}$$

where

ε_{avg} – average heat exchanger effectiveness.
$\dot{m}_{HTF}$ – mass flow rate of HTF.
$c_{p,HTF}$ – specific heat of HTF.
V_{TOT} – total volume of TES unit.
ε_{avg} is defined by authors as shown below:

$$\varepsilon_{avg} = \frac{\overline{T_{HTF,in}} - \overline{T_{HTF,out}}}{\overline{T_{HTF,in}} - T_{PC}} \tag{2}$$

where

$\overline{T_{HTF,in}}$ – average inlet temperature during phase-change process.
$\overline{T_{HTF,out}}$ – average outlet temperature during phase-change process.
T_{PC} – phase change temperature of PCM utilized in the TES unit.
While packing factor Φ_{PCM} is defined as follows:

$$\Phi_{PCM} = \frac{V_{PCM}}{V_{TOT}} \ [-] \tag{3}$$

where

V_{PCM} – volume occupied by PCM.
V_{TOT} – total volume of TES unit.
Parameters for the two experimental regimes ("1.2 lpm" and "1.7 lpm") are presented in Table 3.

The calculated *NHTPC* values are 6.02 for the "1.2 lpm" regime and 8.95 for the "1.7 lpm" regime, reflecting enhanced heat transfer at higher flow rates due to increased convective effects. These results were integrated into the *NHTPC* vs. Φ_{PCM} graph from W. Delgado-Diaz et al. [31], as shown in Fig. 16 (vertical axis on a logarithmic scale).

With a packing factor Φ_{PCM} equal to 0.84 the proposed TES unit

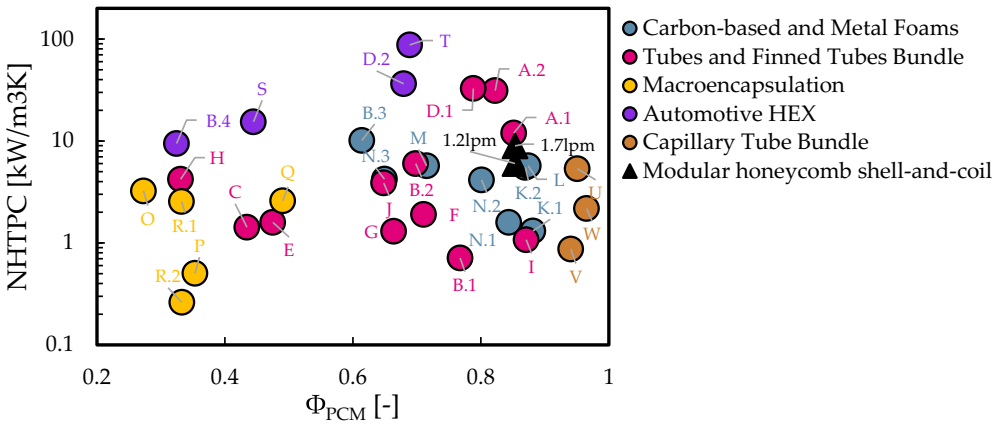

Fig. 16. *NHTPC* vs. Φ_{PCM} for various TES units as presented by W. Delgado-Diaz et al. [31] with added points (black triangles) for honeycomb-shell and coil PCM-based TES unit.

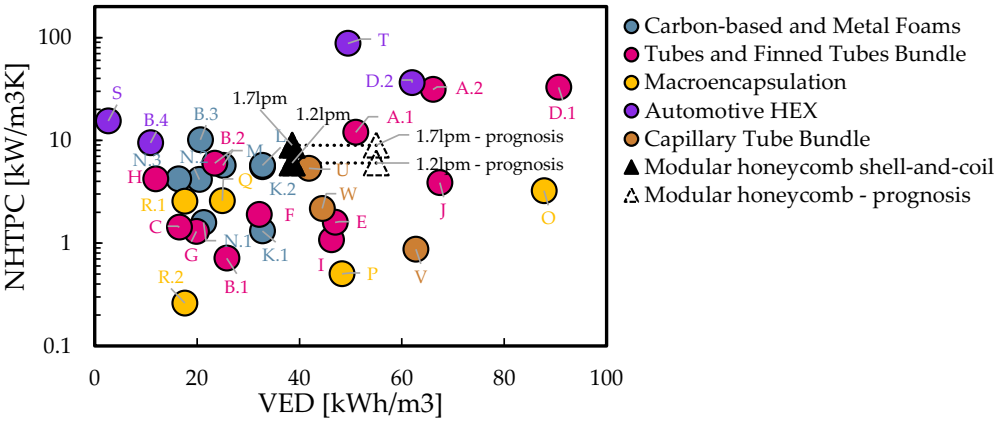

Fig. 17. *NHTPC* vs. *VED* for various TES units as presented by W. Delgado-Diaz et al. [26] with added points (black triangles) for honeycomb-shell and coil PCM-based TES unit. A prognosis for modular TES (dashed triangle) was also added to account for the possibility of PCM change.

demonstrates a high *NHTPC* value compared to most of the 32 configurations analyzed by W. Delgado-Diaz et al. [31]. Only two units, labeled "A.1" and "A.2", exhibit higher *NHTPC* values for a similar Φ_{PCM}, owing to their optimized finned tube arrangements that enhance heat transfer surface area. The proposed unit's performance for "1.7 lpm" regime has *NHTPC* value equal to 8.95, which approaches these benchmarks, indicating competitive heat transfer efficiency despite its modular, non-finned design. The high Φ_{PCM} underscores the unit's ability to maximize PCM utilization within a compact volume, which is a key advantage for scalable applications like solar energy storage. However, the logarithmic scale in Fig. 16 highlights that small differences in *NHTPC* at high Φ_{PCM} values can correspond to significant performance gaps, suggesting potential for further optimization in the proposed design.

To provide a more comprehensive analysis, this study introduces a novel *NHTPC* vs. *VED* graph (shown in Fig. 17), which complements the *NHTPC* vs. Φ_{PCM} methodology by emphasizing energy storage capacity and the unit's compact design. *VED* is calculated as follows:

$$\mathrm{VED} = \frac{\mathrm{m_{PCM}}^{*}\mathrm{H_{ls}}}{\mathrm{V_{TOT}}} \ [-] \tag{4}$$

m_{PCM} – mass of PCM.

H_{ls} – Latent heat of PCM.

The *VED* for both "1.2 lpm" and "1.7 lpm" regimes is 38.56 kWh/m^3, driven by the coconut oil PCM's latent heat. In Fig. 17 the proposed unit's is competitive but lower than several configurations from W. Delgado-Diaz et al. [31], notably macroencapsulated unit "O" and "D.1". These units benefit from the usage of PCMs with significantly higher latent heats, compared to coconut oil's. For instance, unit "O" operates at a high melting point, making it suitable for high-temperature applications, whereas "D.1" uses xylitol, aligning with low-to-medium temperature ranges similar to the proposed unit. The *NHTPC* vs. *VED* graph reveals that "D.1" outperforms "A.1" by nearly a factor of two in *VED*, despite similar *NHTPC* values, highlighting the critical role of PCM selection in achieving high energy density. The proposed unit's *VED*, while lower, reflects the trade-off of using a cost-effective, sustainable PCM like coconut oil, optimized for near-ambient temperature applications.

To explore potential improvements, a prognosis was conducted by hypothetically replacing coconut oil with RT28HC, a commercial PCM with a latent heat of 250 kJ/kg [36] and a similar density, maintaining the packing factor at 0.84. This substitution projects a *VED* increase to approximately 55 kWh/m^3, as shown by the dashed triangles in Fig. 17 for both regimes. This improvement positions the proposed unit closer to high-performance configurations like "D.1" while retaining its modular design advantages. The *NHTPC* vs. *VED* methodology thus provides deeper insights into TES performance by accounting for both heat transfer efficiency and energy storage capacity, addressing limitations in the original *NHTPC* vs. Φ_{PCM} approach, which overlooks PCM thermophysical properties.

To summarize and further contextualize and the proposed unit's performance, comparisons were made with other TES technologies. Microencapsulated PCM systems achieve higher *VED* due to their high PCM loading but are less scalable and more costly, limiting their applicability for large-scale storage. Carbon foam-enhanced TES offers

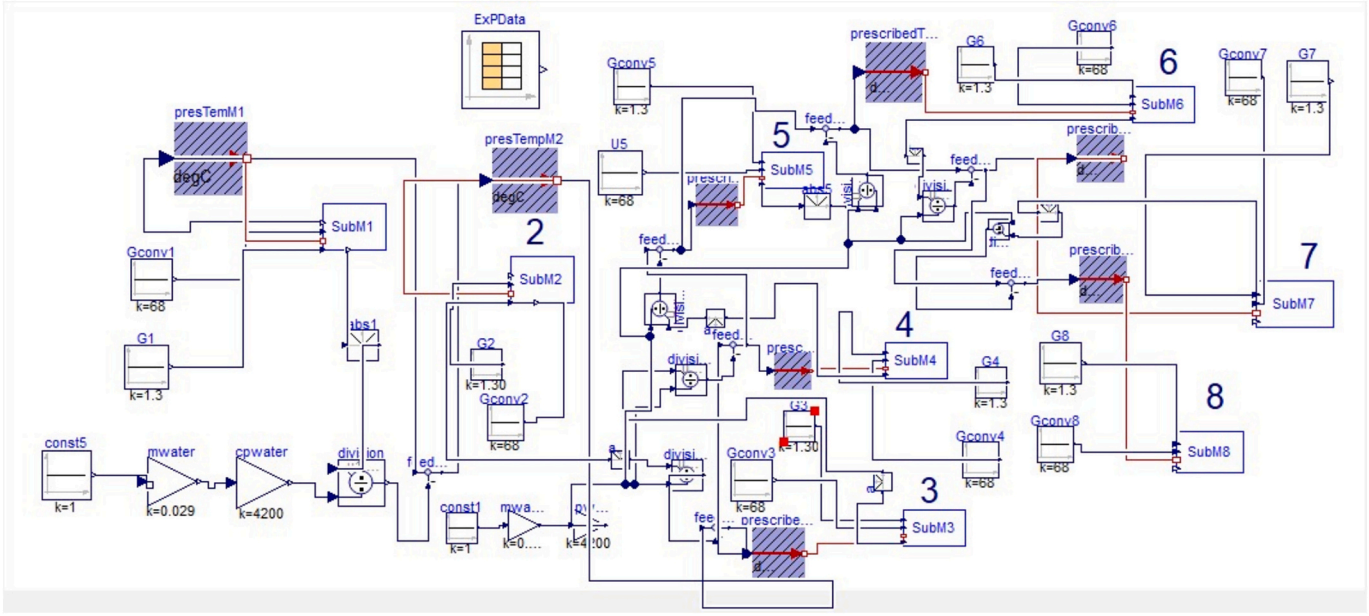

Fig. 18. Model of modular latent TES in Modelica: 1–8 – submodel components, G_{conv} – convective thermal conductance for helical coil side, $G_i = {}^{1}/_{R}$ the inverse of the total thermal resistance for PCM volume [W/K], ExpData – experimental database imported as a timetable.

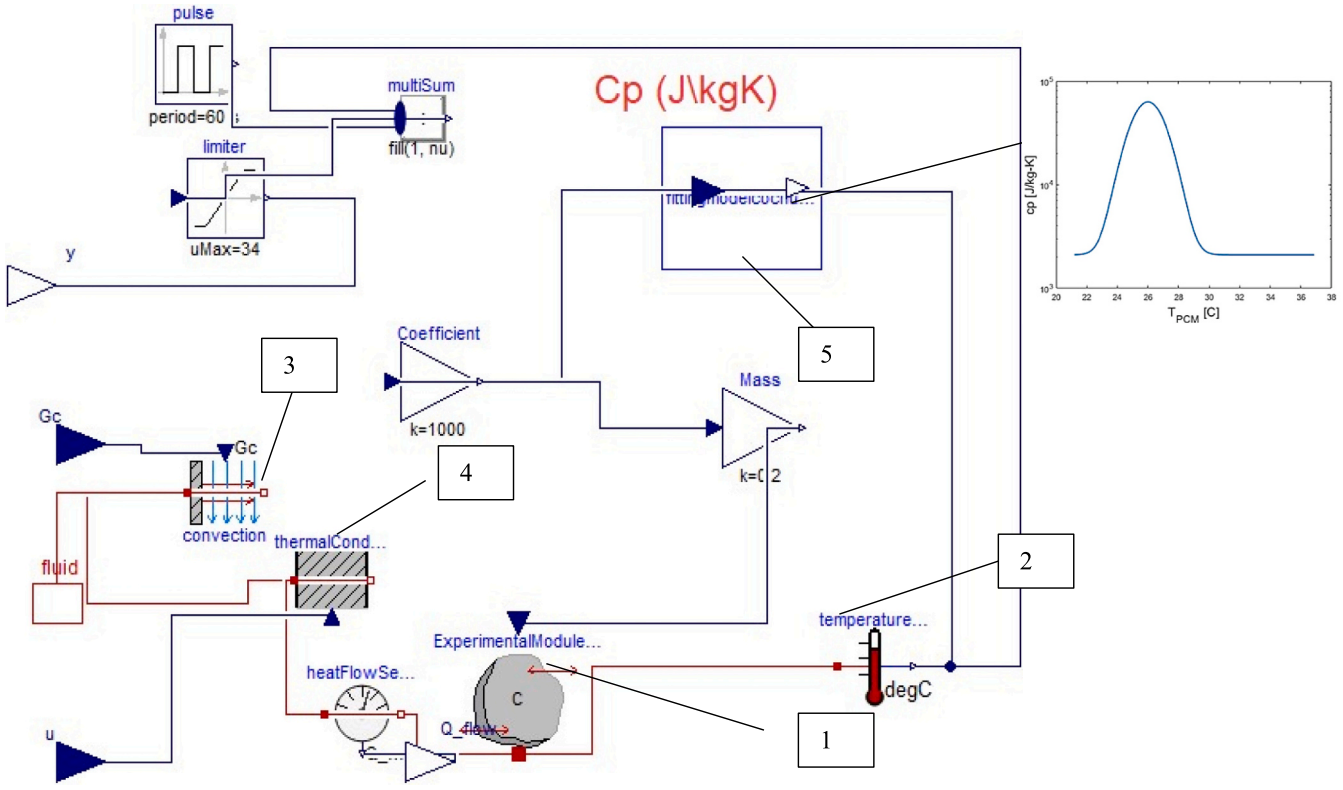

Fig. 19. Schematic diagram of submodel: 1 – model of mass with variable specific heat, 2 – temperature sensor, 3 – model of convection, 4 – model of variable thermal resistance, 5 – model of variable specific heat as a function of temperature of PCM.

superior heat transfer rates by improving thermal conductivity but sacrifices PCM volume, reducing both Φ_{PCM} and *VED*. Tube designs provide higher *NHTPC* through extended heat transfer surfaces but require larger volumes, making them less suitable for compact applications. The proposed honeycomb shell-and-coil TES unit balances compactness, scalability, and performance, making it well-suited for low-temperature applications like solar energy storage and waste heat recovery. Its modular design facilitates easy scaling and maintenance, unlike traditional shell-and-tube or plate-type systems.

Further optimization of heat transfer surface would enhance the proposed unit's *NHTPC* and *VED*. Optimizing the coil geometry for a given cell shape could improve PCM melting uniformity. Modifying the honeycomb cell shape to minimize solid PCM accumulation at the bottom (see Fig. 7) would further accelerate melting, potentially boosting

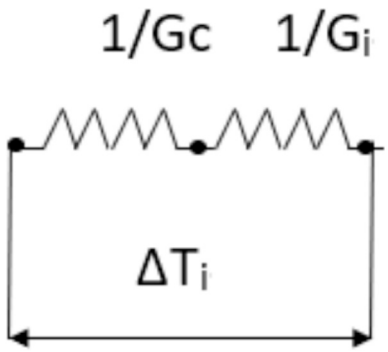

Fig. 20. The thermal resistance network for the heat transfer through a helical coil and PCM volume.

NHTPC without significantly reducing Φ_{PCM}. These optimizations, combined with the proposed *NHTPC* vs. *VED* methodology, position the modular TES unit as a promising candidate for future advancements TES field.

5. Dynamic modeling of LTES using Modelica/Dymola software

Modelica is an object-oriented and equation-based modeling language. What is more, it could be used to simulate complicated systems to improve their design and optimization analysis. The authors previously developed a semi-empirical model of heat transfer during PCM melting/solidification. The objective of this study is to implement experimental results as well as analytical modeling in a Modelica component model and to validate the Modelica calculation results with experimental data. The proposed model is depicted in Fig. 18, Fig. 19, and Fig. 20. The model is composed of unit cells of finite volumes connected in series. Each submodel is connected with the prescribed temperature *PrescTemp*. The temperature at the first cell is constant and equal to the inlet temperature of the propylene glycol during experimental investigations (34 °C). Every next prescribed temperature is calculated as follows:

$$\dot{Q}_i = M_w \bullet c_{p,w} \bullet \Delta T_i \tag{5}$$

$$\Delta T_i = \frac{\dot{Q}_i}{M_w \bullet c_{p,w}} \tag{6}$$

where

$$\Delta T_i = T_{w_{in,i}} - T_{w_{out,i}} \tag{7}$$

$$T_{w_{out,i}} = PrescTemp_i = T_{w\_in,i} - \Delta T_i \tag{8}$$

Each cell (see submodels 1–8 in Fig. 19) was treated as a separate mass with variable specific heat capacity as a function of PCM temperature. The correlation of heat capacity has been obtained experimentally through DSC examination of raw coconut oil [32].

1-D modeling of heat transfer based on total thermal resistance definition was used (see Fig. 20).

Heat is transferred through a lumped thermal element representing convection (linear heat convection model), corresponding to the physics within each helical coil in the module cells. Heat flow depends on convective thermal conductance G_{conv}. That parameter is a function of the heat transfer coefficient (heat transfer coefficient of HTF at helical coil side) and helical coil heat transfer area. The heat transfer coefficient for the helical coil side has been calculated according to correlation from the literature [37]:

$$\overline{Nu} = 0.06 Re^{0.7} Pr^{0.43} \left(\frac{Pr_f}{Pr_w}\right)^{0.25} \left(\frac{d}{D_{coil}}\right)^{0.18} \tag{9}$$

$$h = \frac{\overline{Nu} \bullet \lambda_w}{d_{tube}} \tag{10}$$

Finally:

$$G_{conv} = h \bullet A_{coil} \tag{11}$$

The total thermal resistance within the PCM volume was derived from the author's previous study [32]. In that study average total thermal resistance for melting/solidification of coconut oil in shell and tube geometry was obtained. It has been assumed that total thermal resistance $\overline{R}$ is a function of phase change front thickness δ, average thermal conductivity λ_z and mean heat transfer area $\overline{A}$ (see previous studies [38]).

$$\overline{R} = \frac{\delta}{\lambda_z * \overline{A}} \tag{12}$$

where

$$\overline{A} = \frac{A_2 - A_1}{ln\frac{A_2}{A_1}} \tag{13}$$

A_1 – heat transfer area of tube/helical coil.

A_2 – heat transfer area of the shell.

Finally, assuming that the main parameter that could influence total thermal resistance is heat transfer area such a parameter could be ob-

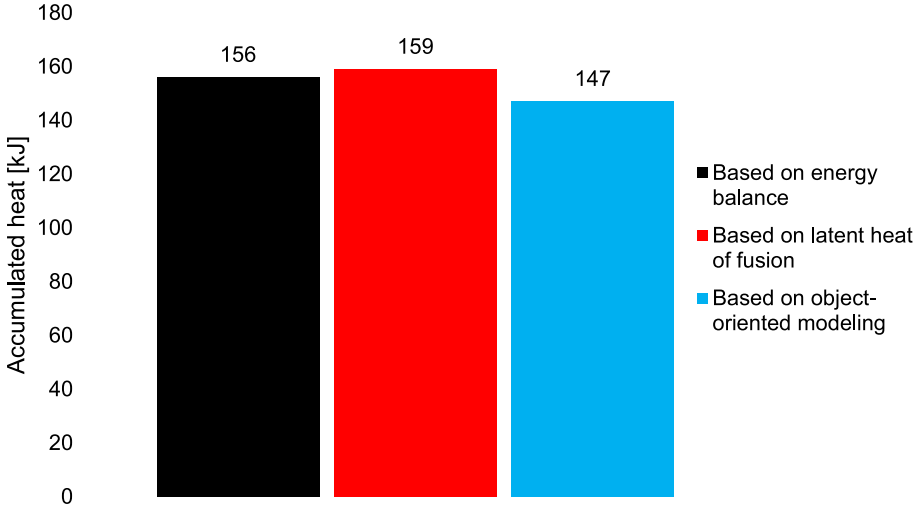

Fig. 21. Comparison of total heat flux accumulated in PCM volume using energy balance.

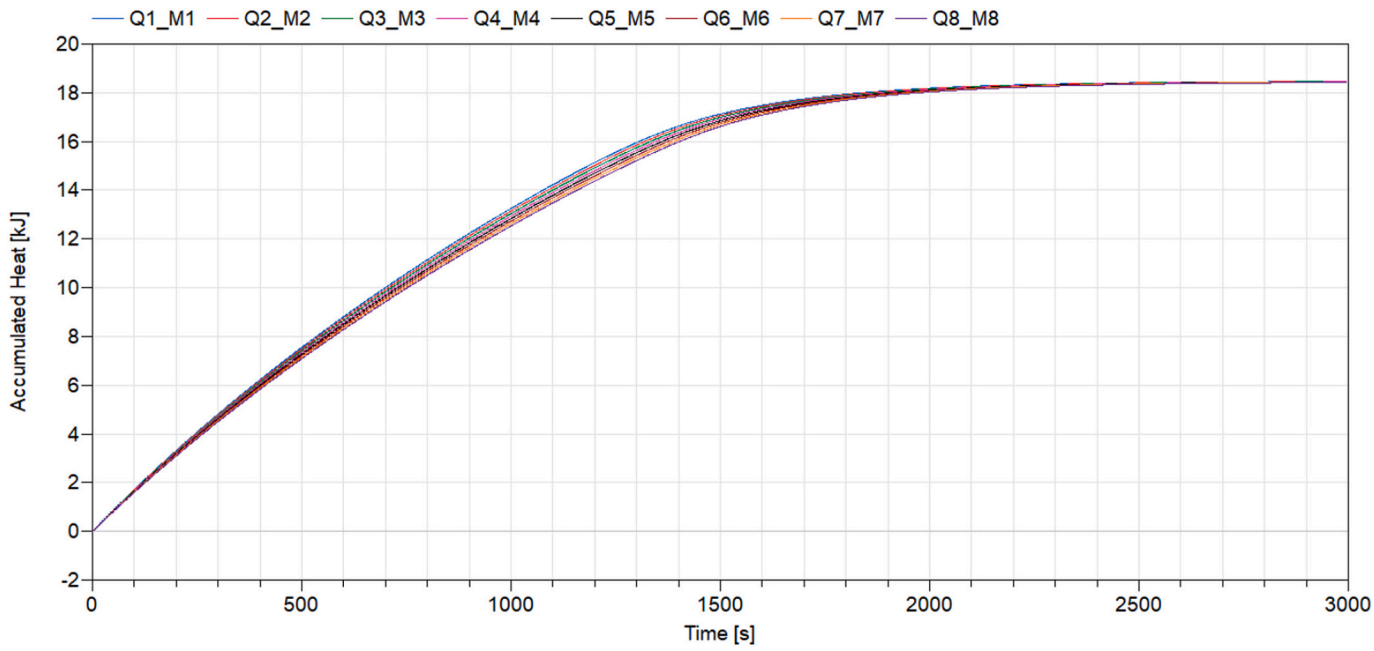

Fig. 22. Accumulated heat vs time for individual cells of the TES module.

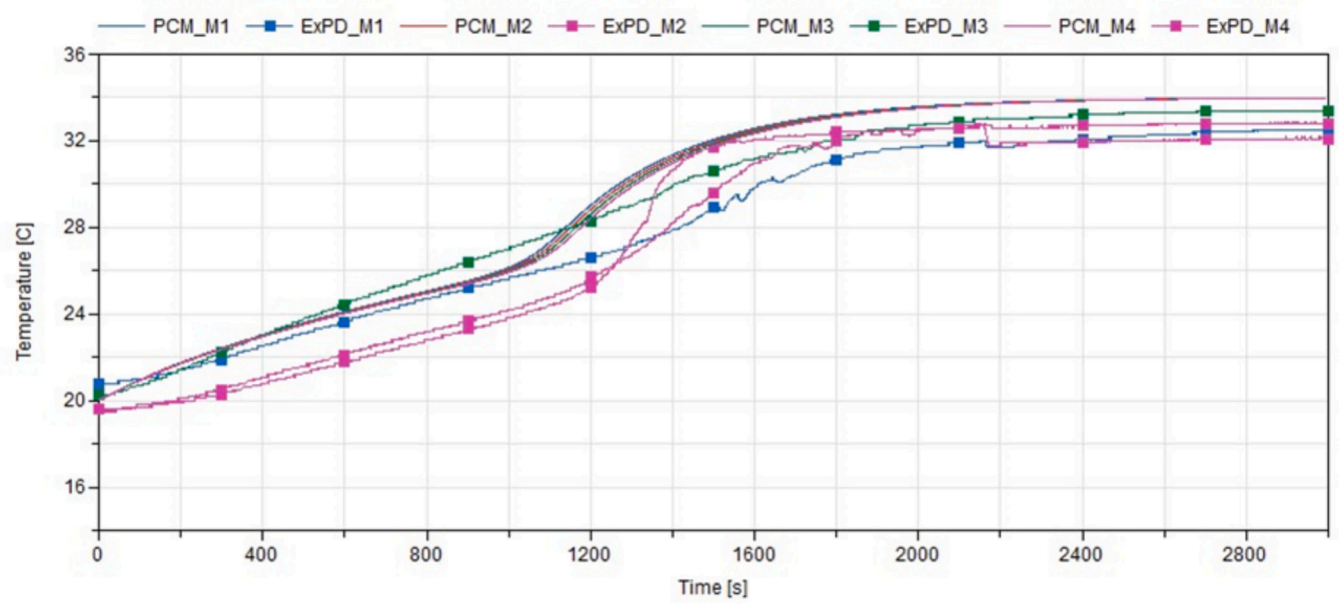

Fig. 23. Comparison of experimental data with model predictions for Cell 1 to 4.

tained for helical coil geometry from the following equation:

$$R_{sc} = \frac{\overline{A}_1}{\overline{A}_2} \bullet R_{sT} = \frac{\overline{A}_1}{\overline{A}_2} \bullet 1.3 = 0.77\ K \Big/ W \tag{14}$$

Then:

$$G_i = \frac{1}{R_{sc}} = 1.3\ W \Big/ K \tag{15}$$

Model predictions were compared with experimental results, showing good agreement. The discrepancy between the total heat flux obtained experimentally from the energy balance of the whole module and obtained from Modelica is not greater than 6 % (see Fig. 21). The Graph for accumulated heat in individual cells as a function of time is shown in Fig. 22.

However, there are some discrepancies between the experimental temperature profiles and predictions of the model from Modelica. Temperature profiles for cells 1–4 are shown in Fig. 23 and temperature profiles for cells 5–8 are shown in Fig. 24. Especially in the case of cells 1–4 the temperature for PCM volume is over-predicted. Experimental temperature curves vary significantly, whereas predicted curves are nearly identical. This is primarily due to the simplification methodology for the estimation of total thermal resistance inside PCM volume. It has been assumed that this parameter is constant, however, it is, first of all, a function of the melting phase (phase change front geometry). Secondly, it should be noted that to simplify calculation only the average temperature for each model has been compared with calculation results. It should be highlighted that this simple methodology could be implemented in rapid engineering calculations to optimize modular LHTES

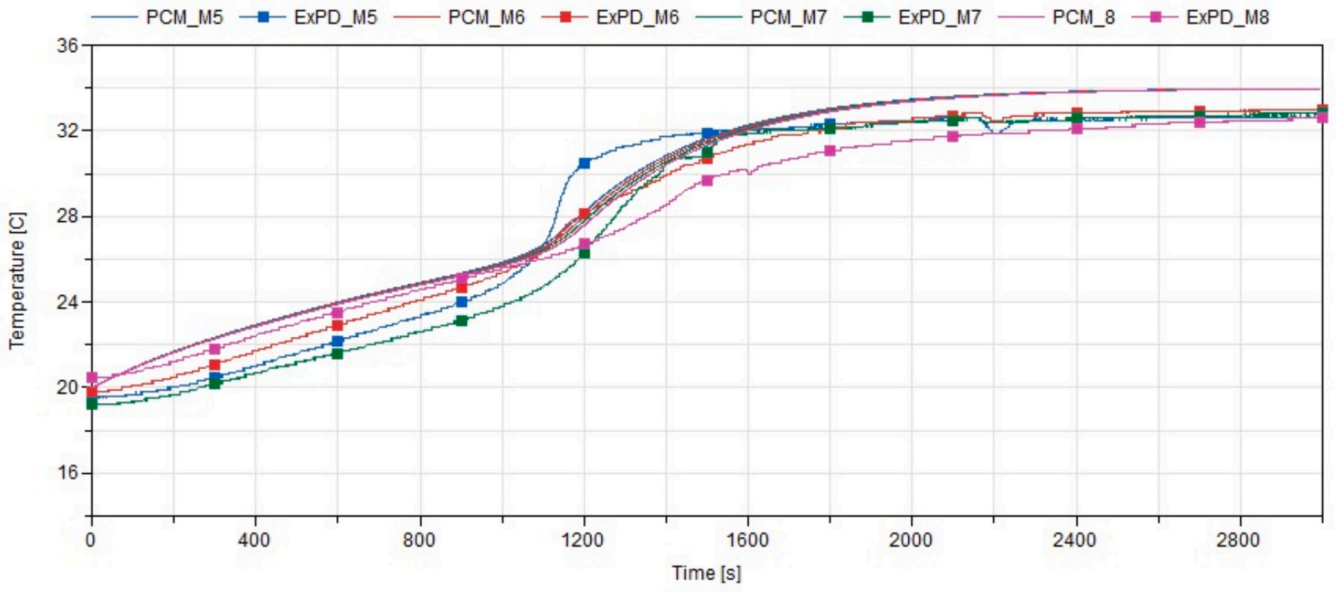

Fig. 24. Comparison of experimental data with model predictions for Cell 5 to 8.

systems. Nevertheless, to better predict the level of charging for each module cell the temperature profiles should be predicted more accurately. Future studies should be focused on developing a theoretical correlation for total thermal resistance within the PCM volume.

6. Conclusions

This study investigates a novel modular, honeycomb shell-and-coil TES unit using coconut oil as the PCM. Extending prior work on single hexagonal-shell TES units [35], the proposed design achieves a *VED* equal to 38.56 kWh/m^3, with potential to reach 55 kWh/m^3 using a higher-latent-heat PCM like RT28HC, as shown in Fig. 17. An experimental database for PCM melting across eight hexagonal cells was validated against a Dymola-based dynamic model, showing a maximum discrepancy of 6 % in accumulated heat (see Fig. 21), confirming the model's reliability for scalable TES design.

A novel *NHTPC* vs. *VED* comparison methodology complements the *NHTPC* vs. Φ_{PCM} approach by W. Delgado-Diaz et al. [31], offering deeper insights into TES performance by integrating heat transfer efficiency and energy storage capacity. This dual framework positions the proposed unit as competitive among 32 configurations, with only two surpassing its NHTPC, and supports a simple engineering tool using total thermal resistance for early-stage design. Future work will develop analytical correlations for variable thermal resistance across diverse geometries and PCMs, enhancing design flexibility.

Experimental results show a 3000 s melting time, consistent with prior findings [35], with natural convection dominating heat transfer. Non-uniform melting in lower cell zones suggests that optimizing coil pitch, shell geometry, and insulation could enhance *NHTPC* and reliability, particularly for rapid-response applications. Compared to microencapsulated PCMs, carbon foam-enhanced systems, shell-and-tube, and plate-type designs, the proposed unit balances compactness and scalability. Addressing heat losses and cell disproportions via improved insulation and parallel HTF flow paths will further improve performance, positioning this modular TES unit as a promising solution for solar energy storage and waste heat recovery. In future work, attention should be focused on intensifying heat transfer in the lower zones of vertical TES.

CRediT authorship contribution statement

Michał Rogowski: Writing – review & editing, Writing – original draft, Visualization, Formal analysis, Data curation. **Maciej Fabrykiewicz:** Writing – original draft, Investigation, Formal analysis. **Dietmar Kuhn:** Writing – review & editing, Software. **Elisabeth Schröder:** Writing – review & editing, Software. **Rafał Andrzejczyk:** Writing – review & editing, Writing – original draft, Supervision, Software, Project administration, Methodology, Funding acquisition, Conceptualization.

Declaration of competing interest

The authors declare that they have no known competing financial interests or personal relationships that could have appeared to influence the work reported in this paper.

Acknowledgments

This research work was supported by the National Centre for Research and Development, Poland (Project No. LIDER/4/0008/L-9/17/NCBR/2018).

Appendix A

Attachment 1. Temperature sensors T0-T8 readings for "1.2 lpm" experimental regime.

Time [s]	T0 [°C]	T1 [°C]	T2 [°C]	T3 [°C]	T4 [°C]	T5 [°C]	T6 [°C]	T7 [°C]	T8 [°C]
0	20,35	19,69	19,65	19,78	19,72	19,45	19,37	19,80	20,64
100	20,84	19,96	20,06	20,13	20,02	19,84	19,71	20,26	20,97
200	21,38	20,36	20,60	20,57	20,51	20,46	20,20	20,81	21,47
300	21,91	20,83	21,20	21,13	21,07	21,07	20,70	21,37	22,07
400	22,40	21,30	21,78	21,65	21,66	21,69	21,20	21,92	22,69
500	22,87	21,82	22,34	22,18	22,21	22,31	21,67	22,38	23,29
600	23,31	22,34	22,91	22,72	22,82	22,97	22,15	22,90	23,89
700	23,70	22,83	23,44	23,21	23,40	23,59	22,64	23,38	24,49
800	24,10	23,29	23,96	23,71	24,04	24,24	23,21	23,84	25,09
900	24,46	23,84	24,53	24,21	24,97	25,03	23,86	24,32	25,68
1000	24,90	24,45	25,26	24,82	26,90	26,19	24,84	24,72	26,40
1100	25,32	25,35	26,16	25,74	30,55	28,16	26,53	25,17	27,62
1200	25,99	27,64	27,29	26,83	31,31	29,94	28,72	26,17	28,90
1300	27,07	30,78	28,50	28,36	31,70	31,07	30,55	28,37	29,78
1400	28,38	31,78	29,71	29,75	31,94	31,67	31,18	30,86	30,41
1500	30,25	32,10	30,69	31,03	32,04	31,84	31,93	31,44	30,40
1600	31,06	32,24	30,91	31,74	32,16	31,97	32,02	31,76	31,80
1700	31,80	32,37	31,55	32,16	32,32	32,14	32,11	32,04	32,24
1800	32,20	32,44	32,59	32,34	32,40	32,28	32,30	32,15	32,49
1900	32,32	32,57	32,65	32,49	32,46	32,39	32,44	32,28	32,67
2000	32,40	32,64	32,72	32,64	32,58	32,46	32,53	32,37	32,79
2100	32,27	31,90	32,91	32,63	31,89	32,03	32,43	32,42	32,89
2200	32,45	31,89	32,90	32,62	32,55	32,29	32,47	32,39	32,93
2300	32,53	31,93	32,93	32,68	32,55	32,49	32,56	32,45	32,97
2400	32,59	32,00	32,97	32,71	32,57	32,57	32,63	32,50	33,02
2500	32,62	32,04	33,01	32,78	32,59	32,65	32,69	32,53	33,06
2600	32,65	32,06	33,05	32,77	32,61	32,67	32,70	32,56	33,11
2700	32,66	32,11	33,05	32,82	32,61	32,68	32,74	32,58	33,15
2800	32,67	32,12	33,07	32,84	32,62	32,71	32,73	32,60	33,19
2900	32,69	32,17	33,06	32,83	32,61	32,70	32,76	32,63	33,21
3000	32,67	32,17	33,05	32,85	32,65	32,73	32,79	32,63	33,23
3100	32,67	32,18	33,09	32,86	32,66	32,75	32,78	32,66	33,26
3200	32,69	32,22	33,08	32,87	32,64	32,76	32,81	32,66	33,29
3300	32,73	32,26	33,10	32,90	32,65	32,77	32,83	32,70	33,33
3400	32,72	32,29	33,09	32,90	32,70	32,78	32,85	32,72	33,37
3500	32,72	32,27	33,09	32,90	32,69	32,77	32,87	32,70	33,39
3600	32,72	32,29	33,07	32,90	32,69	32,78	32,82	32,69	33,40
3700	32,74	32,29	33,07	32,91	32,69	32,78	32,85	32,69	33,41

Attachment 2. Temperature sensors T9-T17 readings for "1.2 lpm" experimental regime.

Time [s]	T9 [°C]	T10 [°C]	T11 [°C]	T12 [°C]	T13 [°C]	T14 [°C]	T15 [°C]	T16 [°C]	T17 [°C]
0	20,32	21,03	20,97	21,83	21,10	21,59	21,79	34,45	29,27
100	20,88	21,95	21,31	22,57	21,78	22,48	22,19	34,46	31,06
200	21,50	22,98	21,83	23,33	22,58	23,34	22,78	34,47	31,46
300	22,10	23,96	22,43	23,99	23,34	24,11	23,39	34,49	32,15
400	22,68	24,89	23,06	24,56	24,05	24,79	23,99	34,50	32,59
500	23,22	25,77	23,69	25,07	24,74	25,43	24,56	34,50	32,64
600	23,73	26,61	24,31	25,55	25,41	26,02	25,09	34,47	32,60
700	24,20	27,48	24,93	25,99	26,04	26,59	25,58	34,44	32,15
800	24,66	28,32	25,54	26,43	26,64	27,12	26,03	34,43	33,58
900	25,09	29,15	26,15	26,82	27,05	27,59	26,43	34,45	33,79
1000	25,52	30,00	26,74	27,14	27,43	28,01	26,81	34,47	33,91
1100	25,89	30,75	27,39	27,44	27,13	28,22	27,23	34,48	33,96
1200	26,28	31,71	28,14	27,68	27,63	28,25	27,55	34,49	34,00
1300	26,97	32,68	28,93	27,87	27,87	28,85	27,75	34,47	34,01
1400	28,05	32,88	30,37	28,16	28,19	29,51	27,85	34,44	34,03
1500	28,71	33,05	31,51	28,34	28,63	29,96	28,15	34,44	34,03
1600	31,27	33,35	31,97	28,50	28,94	30,47	28,52	34,45	34,08
1700	32,38	33,57	32,40	29,02	30,11	31,01	29,39	34,46	34,02
1800	32,74	33,57	32,63	29,44	30,86	31,38	29,83	34,48	34,05
1900	32,96	33,86	32,78	29,77	31,35	31,70	30,16	34,50	34,00
2000	33,10	34,00	32,87	30,05	31,67	32,02	30,42	34,48	33,95
2100	33,23	34,06	32,60	30,42	32,21	31,92	30,19	34,45	33,91
2200	33,32	34,10	32,76	30,62	32,21	32,29	30,61	34,45	33,87
2300	33,38	34,14	32,92	30,82	32,33	32,48	30,83	34,45	33,71
2400	33,43	34,17	33,01	31,11	32,45	32,61	31,02	34,47	33,69
2500	33,48	34,21	33,08	31,39	32,56	32,71	31,20	34,48	33,70
2600	33,52	34,25	33,13	31,58	32,64	32,79	31,36	34,48	33,59
2700	33,55	34,27	33,18	31,72	32,72	32,87	31,50	34,47	33,42
2800	33,58	34,30	33,22	31,84	32,77	32,92	31,61	34,45	33,41
2900	33,60	34,30	33,24	31,93	32,82	32,96	31,69	34,44	33,42
3000	33,62	34,31	33,27	32,01	32,86	32,99	31,75	34,45	33,39

(*continued on next page*)

(*continued*)

Time [s]	T9 [°C]	T10 [°C]	T11 [°C]	T12 [°C]	T13 [°C]	T14 [°C]	T15 [°C]	T16 [°C]	T17 [°C]
3100	33,64	34,32	33,29	32,07	32,90	33,02	31,81	34,47	33,44
3200	33,65	34,34	33,31	32,14	32,93	33,06	31,85	34,49	33,65
3300	33,68	34,36	33,34	32,20	32,97	33,10	31,91	34,50	33,66
3400	33,70	34,38	33,38	32,26	33,00	33,12	31,96	34,48	33,58
3500	33,72	34,39	33,40	32,29	33,03	33,15	32,02	34,45	33,57
3600	33,72	34,40	33,41	32,33	33,05	33,17	32,06	34,46	33,53
3700	33,73	34,40	33,41	32,34	33,05	33,17	32,07	34,46	33,57

Attachment 3. Temperature sensors T0-T8 readings for "1.7 lpm" experimental regime.

Time [s]	T0 [°C]	T1 [°C]	T2 [°C]	T3 [°C]	T4 [°C]	T5 [°C]	T6 [°C]	T7 [°C]	T8 [°C]
0	20,53	19,17	18,77	19,00	19,02	18,43	18,48	19,00	19,54
100	21,47	19,92	18,97	19,22	19,20	18,79	18,96	19,29	19,76
200	22,46	20,57	19,45	19,63	19,56	19,47	19,73	19,85	20,18
300	23,28	21,31	20,00	20,21	20,06	20,26	20,57	20,49	20,80
400	23,86	22,03	20,48	20,80	20,57	20,98	21,36	21,08	21,48
500	24,35	22,78	20,87	21,43	21,09	21,70	22,15	21,66	22,14
600	24,84	23,38	21,27	22,02	21,62	22,33	22,90	22,19	22,80
700	25,44	23,99	21,64	22,62	22,15	22,93	23,60	22,69	23,44
800	25,99	24,57	21,98	23,36	22,74	23,50	24,21	23,18	24,06
900	26,53	25,25	22,28	24,16	23,38	24,10	24,77	23,68	24,67
1000	26,99	26,08	22,72	25,01	24,11	24,74	25,32	24,33	25,30
1100	27,40	27,02	23,22	25,91	24,92	25,43	25,90	25,00	26,02
1200	27,82	28,08	23,91	27,04	25,67	26,25	26,64	25,85	26,84
1300	28,38	30,18	24,69	28,35	26,05	27,10	27,95	26,63	27,70
1400	28,70	30,54	25,37	28,81	27,32	28,08	29,66	27,47	29,11
1500	29,00	30,62	26,20	29,24	28,58	28,91	30,36	27,56	29,63
1600	29,26	30,73	26,99	29,77	30,05	29,86	30,66	27,99	30,09
1700	29,04	30,87	26,22	30,94	30,37	30,64	30,66	28,57	29,92
1800	28,98	31,05	26,17	30,97	30,47	30,95	30,83	30,02	30,68
1900	29,08	31,22	26,35	31,26	30,66	31,12	31,04	30,30	31,26
2000	29,11	31,29	26,54	31,34	30,72	31,16	31,11	30,52	31,49
2100	29,09	31,32	26,66	31,34	30,73	31,17	31,10	30,64	31,67
2200	29,13	31,37	26,86	31,39	30,80	31,26	31,16	30,76	31,77
2300	29,21	31,50	27,07	31,46	30,90	31,38	31,25	30,93	31,83
2400	29,27	31,50	27,25	31,51	30,91	31,45	31,30	30,95	31,89
2500	29,26	31,51	27,40	31,52	30,92	31,47	31,27	30,97	31,94
2600	29,30	31,50	27,52	31,49	30,92	31,48	31,31	31,01	31,97
2700	29,33	31,48	27,64	31,48	30,94	31,52	31,33	31,04	32,00
2800	29,36	31,48	27,75	31,51	31,01	31,50	31,35	31,07	32,02
2900	29,37	31,51	27,80	31,52	31,01	31,50	31,37	31,05	32,03
3000	29,39	31,51	28,08	31,52	31,05	31,50	31,36	31,08	32,07
3100	29,45	31,51	28,23	31,52	31,06	31,51	31,36	31,06	32,12
3200	29,47	31,48	28,27	31,50	31,09	31,53	31,37	31,13	32,16
3300	29,50	31,53	28,04	31,53	31,11	31,56	31,40	31,16	32,20
3400	29,51	31,53	28,57	31,54	31,12	31,58	31,41	31,17	32,23
3500	29,51	31,49	28,90	31,54	31,11	31,57	31,39	31,15	32,26
3600	29,54	31,52	28,89	31,51	31,11	31,53	31,39	31,16	32,29
3700	29,56	31,52	29,02	31,54	31,14	31,54	31,40	31,18	32,33
3800	29,58	31,51	28,97	31,54	31,15	31,57	31,43	31,20	32,37
3900	29,60	31,54	29,24	31,56	31,12	31,57	31,43	31,19	32,40
4000	29,58	31,52	29,12	31,52	31,11	31,56	31,43	31,22	32,42

Attachment 4. Temperature sensors T9-T17 readings for "1.7 lpm" experimental regime.

Time [s]	T9 [°C]	T10 [°C]	T11 [°C]	T12 [°C]	T13 [°C]	T14 [°C]	T15 [°C]	T16 [°C]	T17 [°C]
0	18,99	19,57	20,19	20,85	19,86	20,36	21,15	33,06	29,18
100	19,38	20,08	20,38	21,39	20,24	21,11	21,40	32,87	30,53
200	19,99	21,10	20,74	22,25	20,95	22,25	21,92	32,74	30,83
300	20,64	22,18	21,30	23,05	21,76	23,18	22,60	32,67	31,04
400	21,27	23,22	21,94	23,73	22,56	23,92	23,23	32,65	31,23
500	21,86	24,15	22,60	24,30	23,35	24,56	23,80	32,71	31,05
600	22,42	24,96	23,25	24,81	24,05	25,12	24,30	32,81	31,07
700	22,97	25,67	23,87	25,27	24,66	25,61	24,77	32,93	31,30
800	23,50	26,36	24,43	25,69	25,16	26,06	25,22	33,00	31,51
900	23,99	27,04	24,98	26,06	25,58	26,42	25,58	32,99	31,67
1000	24,45	27,72	25,47	26,39	25,97	26,64	25,92	33,00	31,85
1100	24,90	28,44	26,01	26,68	26,30	26,96	26,22	33,02	32,08

(*continued on next page*)

(*continued*)

Time [s]	T9 [°C]	T10 [°C]	T11 [°C]	T12 [°C]	T13 [°C]	T14 [°C]	T15 [°C]	T16 [°C]	T17 [°C]
1200	25,35	29,63	26,74	26,95	26,54	27,31	26,49	33,03	32,27
1300	25,68	30,45	27,50	27,18	26,78	27,28	26,73	33,01	32,29
1400	26,39	30,89	28,50	27,36	27,06	27,54	26,95	32,94	32,37
1500	27,18	31,61	29,91	27,56	27,25	27,97	26,97	32,91	32,32
1600	28,57	31,94	30,90	27,72	27,35	28,41	27,23	32,92	32,29
1700	30,65	32,28	31,38	27,88	27,52	29,17	27,65	32,95	32,26
1800	31,11	32,54	31,63	28,10	28,06	29,78	28,16	32,95	32,25
1900	31,46	32,66	31,81	28,37	28,97	30,17	28,69	32,92	32,23
2000	31,67	32,71	31,92	28,65	29,68	30,43	29,15	32,92	32,19
2100	31,82	32,77	31,99	28,90	30,10	30,66	29,50	32,94	32,17
2200	31,93	32,82	32,05	29,18	30,40	30,84	29,77	32,97	32,17
2300	32,02	32,88	32,08	29,40	30,63	30,99	29,90	32,98	32,16
2400	32,09	32,92	32,12	29,54	30,83	31,10	30,11	32,94	32,13
2500	32,15	32,91	32,13	29,71	30,97	31,21	30,26	32,93	32,13
2600	32,18	32,91	32,14	29,86	31,11	31,33	30,40	32,95	32,09
2700	32,22	32,93	32,15	30,02	31,23	31,43	30,49	32,97	32,13
2800	32,26	32,95	32,17	30,20	31,34	31,52	30,57	32,96	32,14
2900	32,28	32,97	32,19	30,41	31,43	31,58	30,66	32,92	32,19
3000	32,30	32,97	32,19	30,59	31,50	31,62	30,74	32,92	32,21
3100	32,31	32,99	32,20	30,74	31,56	31,66	30,80	32,94	32,26
3200	32,32	32,98	32,20	30,86	31,60	31,70	30,85	32,97	32,30
3300	32,34	33,00	32,22	30,95	31,64	31,73	30,90	32,95	32,32
3400	32,35	33,02	32,24	31,03	31,66	31,76	30,94	32,92	32,33
3500	32,37	33,03	32,24	31,12	31,69	31,79	31,00	32,93	32,35
3600	32,38	33,03	32,26	31,21	31,73	31,83	31,05	32,96	32,40
3700	32,40	33,05	32,28	31,29	31,77	31,86	31,11	32,98	32,46
3800	32,42	33,07	32,31	31,36	31,81	31,90	31,16	32,96	32,50
3900	32,44	33,08	32,32	31,41	31,84	31,93	31,20	32,93	32,52
4000	32,45	33,08	32,34	31,47	31,87	31,95	31,24	32,95	32,56

Data availability

Data will be made available on request.

References

[1] H. Selvnes, Y. Allouche, R.I. Manescu, A. Hafner, Review on Cold Thermal Energy Storage Applied to Refrigeration Systems using Phase Change Materials, Elsevier Ltd, May 01, 2021, https://doi.org/10.1016/j.tsep.2020.100807.

[2] H. Rezaei, M.J. Ghomsheh, F. Kowsary, P. Ahmadi, Performance assessment of a range-extended electric vehicle under real driving conditions using novel PCM-based HVAC system, Sustain. Energy Technol. Assess. 47 (Oct. 2021), https://doi.org/10.1016/j.seta.2021.101527.

[3] N. Javani, I. Dincer, G.F. Naterer, B.S. Yilbas, Heat transfer and thermal management with PCMs in a Li-ion battery cell for electric vehicles, Int. J. Heat Mass Transf. 72 (2014) 690–703, https://doi.org/10.1016/j.ijheatmasstransfer.2013.12.076.

[4] M.E. Zayed, et al., Applications of cascaded phase change materials in solar water collector storage tanks: a review, Sol. Energy Mater. Sol. Cells 199 (Sep. 2019) 24–49, https://doi.org/10.1016/j.solmat.2019.04.018.

[5] P. Royo, L. Acevedo, V.J. Ferreira, T. García-Armingol, A.M. López-Sabirón, G. Ferreira, High-temperature PCM-based thermal energy storage for industrial furnaces installed in energy-intensive industries, Energy 173 (Apr. 2019) 1030–1040, https://doi.org/10.1016/j.energy.2019.02.118.

[6] M. Singh, J. Bhattacharya, Experimental demonstration of the thermodynamic advantage of modular heat storage system for a variable-temperature input, Therm. Sci. Eng. Progress 13 (Oct. 2019), https://doi.org/10.1016/j.tsep.2019.100399.

[7] K. Kant, P.H. Biwole, A. Shukla, A. Sharma, S. Gorjian, Heat transfer and energy storage performances of phase change materials encapsulated in honeycomb cells, J. Energy Storage 38 (Jun. 2021), https://doi.org/10.1016/j.est.2021.102507.

[8] M. Abuşka, S. Şevik, A. Kayapunar, Experimental analysis of solar air collector with PCM-honeycomb combination under the natural convection, Sol. Energy Mater. Sol. Cells 195 (Jun. 2019) 299–308, https://doi.org/10.1016/j.solmat.2019.02.040.

[9] M. Abuşka, S. Şevik, A. Kayapunar, A comparative investigation of the effect of honeycomb core on the latent heat storage with PCM in solar air heater, Appl. Therm. Eng. 148 (Feb. 2019) 684–693, https://doi.org/10.1016/j.applthermaleng.2018.11.056.

[10] A. Andreozzi, B. Buonomo, D. Ercole, O. Manca, Solar energy latent thermal storage by phase change materials (PCMs) in a honeycomb system, Therm. Sci. Eng. Progress 6 (Jun. 2018) 410–420, https://doi.org/10.1016/j.tsep.2018.02.003.

[11] A. Andreozzi, B. Buonomo, D. Ercole, O. Manca, Phase change materials (PCMs) in a honeycomb system for solar energy applications, Int. J. Heat Technol. 35 (Special Issue 1) (Sep. 2017) S472–S477, https://doi.org/10.18280/ijht.35Sp0164.

[12] M.S. Mahdi, A.F. Hasan, Numerical study on the thermal energy storage employing phase change material with honeycomb structure: the effect of heat transfer fluid configuration and honeycomb cell angles, Energy Storage 5 (1) (Feb. 2023), https://doi.org/10.1002/est2.396.

[13] S.A. Sadri, H. Parsa, M. Saffar-Avval, M.R. Hajmohammadi, Configuration optimization of the honeycomb core in the latent heat thermal energy storage of a solar air heater: experimental and numerical study, Int. J. Energy Res. 46 (5) (Apr. 2022) 5924–5954, https://doi.org/10.1002/er.7532.

[14] R. Hirmiz, H.M. Teamah, M.F. Lightstone, J.S. Cotton, Performance of heat pump integrated phase change material thermal storage for electric load shifting in building demand side management, Energ. Build. 190 (May 2019) 103–118, https://doi.org/10.1016/j.enbuild.2019.02.026.

[15] A. Gil, G. Peiró, E. Oró, L.F. Cabeza, Experimental analysis of the effective thermal conductivity enhancement of PCM using finned tubes in high temperature bulk tanks, Appl. Therm. Eng. 142 (Sep. 2018) 736–744, https://doi.org/10.1016/j.applthermaleng.2018.07.029.

[16] S. Abbas, Z. Ramadan, C.W. Park, Thermal performance analysis of compact-type simulative battery module with paraffin as phase-change material and flat plate heat pipe, Int. J. Heat Mass Transf. 173 (Jul. 2021), https://doi.org/10.1016/j.ijheatmasstransfer.2021.121269.

[17] G. Dogkas, et al., Development and experimental testing of a compact thermal energy storage tank using paraffin targeting domestic hot water production needs, Therm. Sci. Eng. Progress 19 (Oct. 2020), https://doi.org/10.1016/j.tsep.2020.100573.

[18] R.M. Saeed, J.P. Schlegel, R. Sawafta, V. Kalra, Plate type heat exchanger for thermal energy storage and load shifting using phase change material, Energy Convers. Manag. 181 (Feb. 2019) 120–132, https://doi.org/10.1016/j.enconman.2018.12.013.

[19] M. Fadl, P.C. Eames, An experimental investigation of the heat transfer and energy storage characteristics of a compact latent heat thermal energy storage system for domestic hot water applications, Energy 188 (Dec. 2019), https://doi.org/10.1016/j.energy.2019.116083.

[20] M.M. Joybari, S. Seddegh, X. Wang, F. Haghighat, Experimental investigation of multiple tube heat transfer enhancement in a vertical cylindrical latent heat thermal energy storage system, Renew. Energy 140 (Sep. 2019) 234–244, https://doi.org/10.1016/j.renene.2019.03.037.

[21] S. Tiari, M. Mahdavi, S. Qiu, Experimental study of a latent heat thermal energy storage system assisted by a heat pipe network, Energy Convers. Manag. 153 (Dec. 2017) 362–373, https://doi.org/10.1016/j.enconman.2017.10.019.

[22] S. Seddegh, X. Wang, M.M. Joybari, F. Haghighat, Investigation of the effect of geometric and operating parameters on thermal behavior of vertical shell-and-tube latent heat energy storage systems, Energy 137 (2017) 69–82, https://doi.org/10.1016/j.energy.2017.07.014.

[23] M. Esapour, M.J. Hosseini, A.A. Ranjbar, Y. Pahamli, R. Bahrampoury, Phase change in multi-tube heat exchangers, Renew. Energy 85 (Jan. 2016) 1017–1025, https://doi.org/10.1016/j.renene.2015.07.063.

[24] A. Pourakabar, A.A. Rabienataj Darzi, Enhancement of phase change rate of PCM in cylindrical thermal energy storage, Appl. Therm. Eng. 150 (Mar. 2019) 132–142, https://doi.org/10.1016/j.applthermaleng.2019.01.009.
[25] M. Rogowski, R. Andrzejczyk, Recent advances of selected passive heat transfer intensification methods for phase change material-based latent heat energy storage units: a review, Int. Commun. Heat Mass Transf. 144 (May 2023) 106795, https://doi.org/10.1016/j.icheatmasstransfer.2023.106795.
[26] R. Andrzejczyk, T. Muszynski, T. Kowalczyk, M. Saqib, Experimental and numerical investigation on shell and coil storage unit with biodegradable PCM for modular thermal battery applications, Int. J. Therm. Sci. 185 (Mar. 2023), https://doi.org/10.1016/j.ijthermalsci.2022.108076.
[27] W.B. Ye, M. Arıcı, 3D validation, 2D feasibility, corrected and developed correlations for pure solid-gallium phase change modeling by enthalpy-porosity methodology, Int. Commun. Heat Mass Transf. 144 (May 2023), https://doi.org/10.1016/j.icheatmasstransfer.2023.106780.
[28] W.B. Ye, M. Arıcı, False diffusion, asymmetrical interface, and equilibrious state for pure solid-gallium phase change modeling by enthalpy-porosity methodology, Int. Commun. Heat Mass Transf. 144 (May 2023), https://doi.org/10.1016/j.icheatmasstransfer.2023.106746.
[29] W.B. Ye, M. Arıcı, Redefined interface error, 2D verification and validation for pure solid-gallium phase change modeling by enthalpy-porosity methodology, Int. Commun. Heat Mass Transf. 147 (Oct. 2023), https://doi.org/10.1016/j.icheatmasstransfer.2023.106952.
[30] W.B. Ye, M. Arıcı, Exploring mushy zone constant in enthalpy-porosity methodology for accurate modeling convection-diffusion solid-liquid phase change of calcium chloride hexahydrate, Int. Commun. Heat Mass Transf. 152 (Mar. 2024), https://doi.org/10.1016/j.icheatmasstransfer.2024.107294.
[31] W. Delgado-Diaz, A. Stamatiou, S. Maranda, R. Waser, J. Worlitschek, Comparison of heat transfer enhancement techniques in latent heat storage, Appl. Sci. (Switzerl.) 10 (16) (Aug. 2020), https://doi.org/10.3390/app10165519.
[32] R. Andrzejczyk, T. Kowalczyk, P. Kozak, T. Muszyński, Experimental and theoretical study of a vertical tube in shell storage unit with biodegradable PCM for low temperature thermal energy storage applications, Appl. Therm. Eng. 183 (Jan. 2021), https://doi.org/10.1016/j.applthermaleng.2020.116216.
[33] M. Rogowski, M. Fabrykiewicz, P. Szymański, R. Andrzejczyk, The in-house method of manufacturing a low-cost heat pipe with specified Thermophysical properties and geometry, Appl. Sci. 13 (14) (Jul. 2023) 8415, https://doi.org/10.3390/app13148415.
[34] M. Macagnan, M.H. Macagnan, J.B. Copetti, R. Bueno De Souza, R.K. Reichert, M. Amaro, Analysis of the influence of refrigerant charge and compressor duty cycle in an automotive air conditioning system, in: Conference: 22nd International Congress of Mechanical Engineering (COBEM 2013), 2013 [Online]. Available: https://www.researchgate.net/publication/273762891.
[35] R. Andrzejczyk, T. Muszyński, M. Fabrykiewicz, M. Rogowski, Heat transfer enhancement of modular thermal energy storage unit for reversible heat pump cooperation, Int. J. Therm. Sci. 193 (Nov. 2023), https://doi.org/10.1016/j.ijthermalsci.2023.108498.
[36] Rubitherm Technologies GmbH, RT28HC – Technisches Datenblatt, 2025.
[37] Y.A. Kuzma-Kichta, Heat Transfer in Coiled Tubes. Thermopedia, 2025.
[38] R. Andrzejczyk, M. Saqib, T. Kowalcyzk, H.M. Ali, Study on effective front region thickness of PCM in thermal energy storage using a novel semi-theoretical model, Int. Commun. Heat Mass Transf. 146 (Jul. 2023), https://doi.org/10.1016/j.icheatmasstransfer.2023.106901.